

Blockage effect influence on model-scale marine propeller performance and cavitation pattern

Eduardo Tadashi Katsuno^{a,*}, João Lucas Dozzi Dantas^b

^aUniversity of São Paulo, Escola Politécnica, Department of Mechatronics and Mechanical Systems Engineering, 2231 Prof. Mello Moraes Ave., São Paulo, 05508-030, São Paulo, Brazil, orcid.org/0000-0003-2818-3518

^bInstitute for Technological Research, Energy and Infrastructure Laboratory, 532 Prof. Almeida Prado Ave., São Paulo, 05508-901, São Paulo, Brazil, orcid.org/0000-0002-6482-0222

Abstract

The blockage effect is one of the drawbacks in the use of cavitation tunnels, which may considerably interfere in the measurements of the hydrodynamics of model-scale propellers. The literature presents some methods to correct the acquired values, such as the Glauert method, but the deduction of this method does not consider the cavitation effects. This paper aims to use CFD tools to compare and analyze the effect of different levels of blockages on the thrust, torque, hydrodynamic efficiency, and cavitation on two model-scale marine propellers. Five different blockage ratios (from 1% to 41%) and three test cases are simulated, varying the advance ratio to compose the propeller performance diagram. The simulations have shown that the Glauert formula satisfactorily corrected thrust, torque, and hydrodynamic efficiency, even in moderate cavitation. When cavitation is intense, it is observed that the blockage decreases the thrust and torque, not being recommended to use the Glauert formula. It is observed that the cavitation is sensitive to blockage, and it can affect its pattern on the blade surface.

*Corresponding author, eduardo.katsuno@gmail.com

Email addresses: eduardo.katsuno@gmail.com (Eduardo Tadashi Katsuno), jdantas@ipt.br (João Lucas Dozzi Dantas)

Nomenclature

C_p	Pressure coefficient
D_p	Propeller diameter
d	Dimension of the numerical cavitation tunnel
E	Comparison error
h	Characteristic length
J	Advance ratio
K_T	Thrust coefficient
$K_{T,s}, K_{T,p}, K_{T,h}$	Thrust coefficient from the suction face, pressure face, and hub
K_Q	Torque coefficient
n	Rotation rate
N_e	Number of elements
p_{cav}	Percentage of the propeller suction face covered by cavitation
p_h	Hydrostatic pressure
p_s	Saturation pressure
Q	Torque
Re_p	Propeller-based Reynolds number
r	Cell size ratio, $r = h/h_{finest}$
U_{val}	Validation uncertainty
T	Thrust force
v_a	Advance velocity
α	Blockage ratio
η_0	Hydrodynamic efficiency
μ	Dynamic viscosity
ρ	Density
σ	Cavitation index

1. Introduction

Cavitation tunnels are used in naval and ocean engineering to investigate the hydrodynamics of propellers and rudders, including conditions with significant cavitation. One of the main drawbacks of these devices is the so-called blockage effect, which is when the streamflow is affected by the presence of tunnel walls, interfering with the hydrodynamics of the studied body. One way to estimate the blockage influence is to compare the measured force and torque from the cavitation tunnel with those obtained on a large towing tank. However, as the majority of towing tanks do not control the static pressure of the experiments, it is not possible to predict the cavitation pattern for low

8 hydrostatic conditions.

9 The blockage effect is well-known and studied in several experimental fields these days, such as the blockage into
10 the ventilated tunnel fires (Meng et al., 2020) or in the automotive industry, when testing vehicles with wind tunnels
11 (Fischer et al., 2010; Collin et al., 2016). More recently, Ljungskog et al. (2020) discusses and compares the effect
12 of the blockage of the strolled wall wind tunnel test section geometry to a sedan car using CFD (Computational Fluid
13 Dynamics) simulation. For the wind turbines, the topic is present in several parts of the project: assessing the blockage
14 of an analytical wind farm (Segalini, 2021), tip vortices (Soto-Valle et al., 2020), or in test with micro wind turbines
15 (Shirzadeh et al., 2021). Branlard and Meyer Forsting assesses the blockage of wind farms, discussing that neglecting
16 blockage effects typically leads to an overestimation of the production. However, the blockage can be explored to
17 enhance the turbine performance, such as in rivers and tidal channels (Espina-valdés et al., 2020). Ross and Polagye
18 (2020) states that the research of blockage effect into the field of wind turbines is motivated because turbine testings
19 conducted in laboratory facilities or numerical simulations usually have finite domains.

20 In towing tank tests, aiming to test a model-scale vessel, the International Towing Tank Conference (ITTC, 2011a)
21 describes three methods, Schuster, Scott, and Tamura (further described in the reference), to correct the blockage
22 effect for deep-water resistance, sinkage, and trim results. It is discussed the preference for correction expressed as
23 an adjustment of speed, showing that the Scott correction tends to fit most of the data best, being recommended for
24 general use of towing tank experiments, with some limitations related to the Froude number, model length, and depth
25 ratio.

26 Glauert (1983) proposes a one-dimensional potential formulation to correct the effect of wind tunnel interference
27 when a propeller is tested, being widely used for blockage correction (Barlow et al., 1999; Deters et al., 2014). More
28 recently, Mikkelsen and Sørensen (2002) and Sorensen et al. (2006) applied CFD techniques to model the wind tunnel
29 blockage effects to compare the results with Glauert's blockage correction. The conclusions show that the correction
30 is in particularly good agreement with the computation, ensuring the reliability of the one-dimensional momentum
31 theory wall correction. Ryi et al. (2015) discusses the blockage effect of a horizontal-axis wind turbine and proposes
32 a correction algorithm for the original Glauert method to process the data with three different wind tunnel sizes. It is
33 observed that the correction method is appropriate for low-thrust conditions, but not with perfect correction for higher
34 thrust conditions. For the maritime field, ITTC (2017, 2016) describe some recommended procedures and guidelines
35 for model-scale propeller tests, such as blockage ratios less than 20%. Zilic de Arcos et al. (2020) uses CFD tools to
36 compare six different blockage correction methods for axial-flow tidal turbines.

37 Regarding the blockage effect into the cavitation phenomena, Balachandar and Ramamurthy (1991) discusses the
38 cavitation inception considering two-dimensional bluff bodies subjected to wall interference effects and providing
39 some experimental results. It is concluded that for sharp-edged bluff bodies the cavitation inception is weakly de-
40 pendent on the Reynolds number and closely related to blockage effects. For marine propellers, a condition of high
41 thrust in low hydrostatic pressure may lead to cavitation. Thus, it is also important to consider the blockage effect
42 for the cavitation pattern analysis. Using a lifting-surface vortex-lattice method, Choi and Kinnas (1999) resolves

43 an unsteady flow of a cavitating propeller considering the blockage effect, comparing the results with experimental
44 results. Watanabe and Brennen (2003) investigates the unsteady dynamics and instabilities of cavitating propellers
45 operating in a cavitation tunnel, analyzing the effect of tunnel walls on the promotion of the surge of instabilities.
46 Lee and Kinnas (2005) applies the boundary element method to a marine propeller subject to a non-axisymmetric
47 inflow with the blockage effect. Besides the increase of thrust and torque coefficients, the blockage effect also affects
48 the volume of cavitation. Using CFD tools, a previous study was started in Katsuno and Dantas (2017), but a deep
49 analysis of the blockage effects into cavitating propellers was not approached, especially on the condition of severe
50 cavitation.

51 Deep analysis on the blockage correction for marine propeller applications in cavitating conditions is relevant
52 as most of the cited blockage corrections were developed and studied for wind applications. Thus, cavitation is not
53 considered in these analyses, being important to check if the blockage correction is valid, and up to which conditions,
54 for cavitating operations. Indeed, for tidal turbines rotors, Wimshurst et al. (2018) states that the blockage effect is
55 currently not accounted for cavitation analysis.

56 Aiming to evaluate the effectiveness of the blockage correction on a marine propeller in cavitation tunnel tests,
57 especially when cavitation is considerable, this paper aims to use CFD tools to analyze the effect of different blockage
58 ratios on the thrust, torque, hydrodynamic efficiency, and cavitation area. Experiments are conducted at the Institute
59 for Technological Research's (IPT) Cavitation Tunnel to ensure that the adopted numerical method is accurate, by
60 conducting the Verification and Validation (V&V) procedure, estimating the experimental and numerical uncertain-
61 ties. Then, the investigation is conducted using CFD to simulate two different propellers in three different test case
62 scenarios and five blockage ratios, changing the cavitation indices and the advance velocities, observing the blockage
63 influence on the propeller performance indicators and cavitation on the blade. The results are compared before and
64 after applying the blockage correction, evaluating its effectiveness to minimize distortions due to the blockage.

65 **2. Methods**

66 *2.1. Test case propellers and coefficients*

67 Two propellers are tested, being named in this paper as P104 and P107, as shown in Fig. 1.

68 The propeller P104 is a 1:7 model-scale propeller for a 200-ton boat, designed to operate between 10 and 16 knots
69 in fresh and salt water. The propeller design is based on a Gawn-Burril (KCA) systematic series (Gawn and Burril,
70 1957). P104 has three blades, and the full-scale propeller has a diameter of 1400 mm. This model-scale has a diameter
71 of 200 mm, pitch-to-diameter ratio of 0.86, expanded area ratio of 0.50, and axis diameter of 0.038 m, as shown in
72 Fig. 2 and Fig. 3. Note that the propeller has a rounded tip, smoothing out the propeller edges. The hub and axis are
73 represented in all simulations to get higher similarity with experimental tests.

74 The propeller P107 is a 1:1.588 model-scale propeller, designed using the nominal wake of the DARPA Suboff
75 Submarine (Groves et al., 1989), aiming to have a maximum diameter of 59% of the diameter of the resistant hull. The

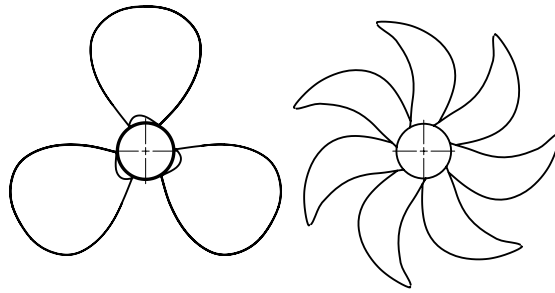


Figure 1: Test case propellers, named P104 (left) and P107 (right).

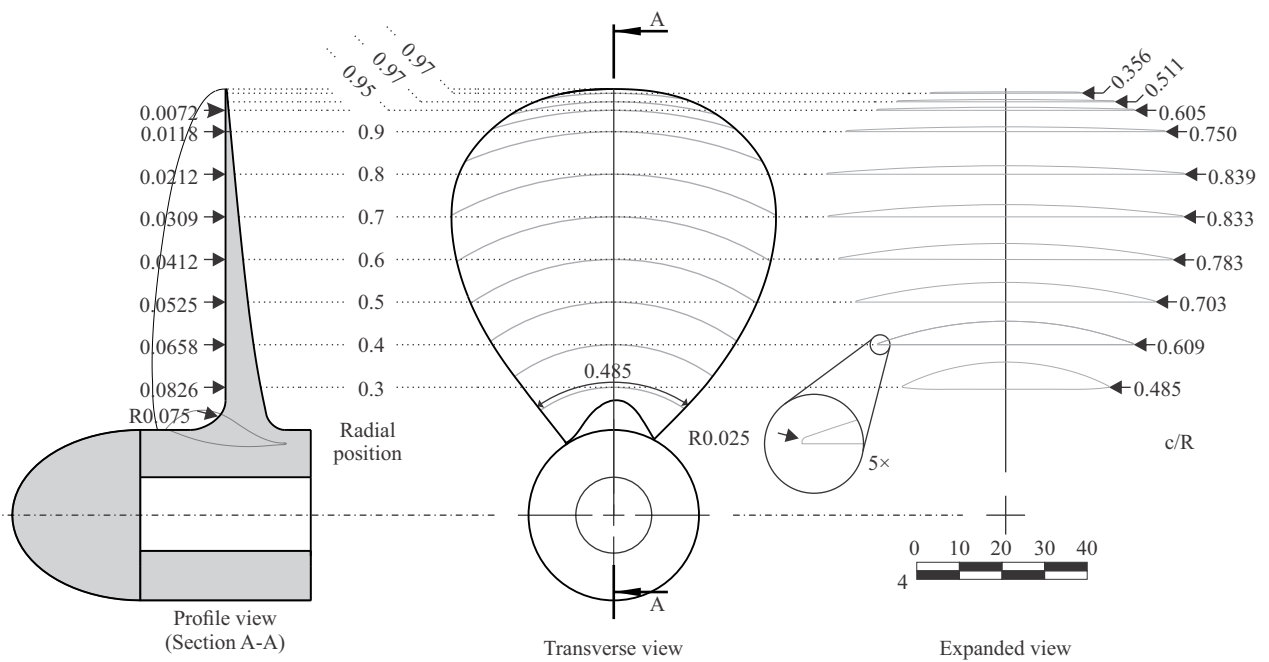


Figure 2: Profile, transverse and expanded view of the propeller P104 (units in m).

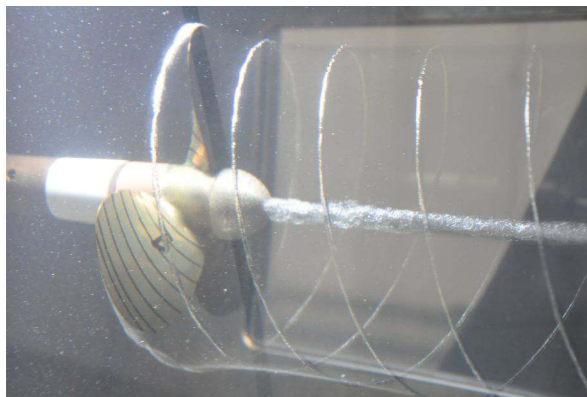


Figure 3: Propeller P104 inside the IPT's Cavitation Tunnel.

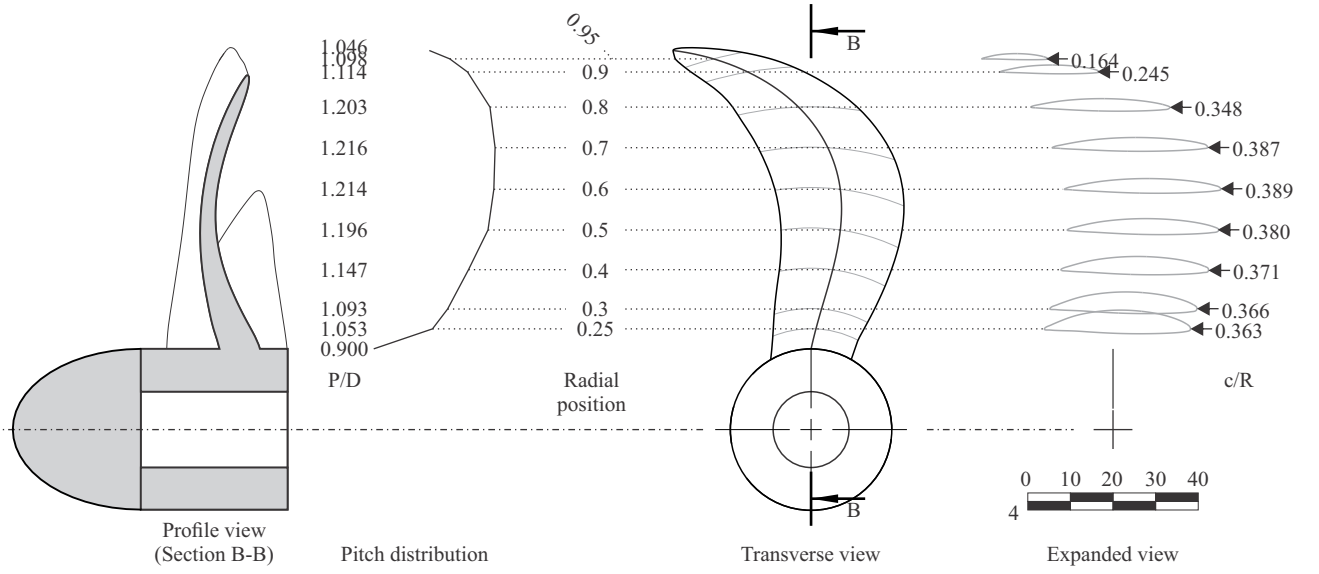


Figure 4: Profile, pitch-to-diameter (P/D) distribution, transverse, and expanded view of the propeller P107 (units in m).

76 design procedure can be found in Sbragio (1995). P107 has seven blades, and the full-scale propeller has a diameter
 77 of 300 mm. This model-scale has a diameter of 189 mm, pitch-to-diameter ratio of 1.216, expanded area ratio of
 78 0.60374, skew angle of 28° , as shown in Fig. 4.

79 The operating conditions are expressed through three coefficients: advance ratio J , cavitation index σ , and
 80 propeller-based Reynolds number Re_p :

$$J = \frac{v_a}{nD_p}, \quad \sigma = \frac{p_h - p_s}{\frac{1}{2}\rho(nD_p)^2}, \quad Re_p = \frac{\rho n D_p^2}{\mu}. \quad (1)$$

81 The analyzed outputs correspond to typical propeller performance indicators, namely thrust coefficient K_T , torque
 82 coefficient K_Q , and hydrodynamic efficiency η_0 . These properties are expressed as:

$$K_T = \frac{T}{\rho n^2 D_p^4}, \quad K_Q = \frac{Q}{\rho n^2 D_p^5}, \quad \eta_0 = \frac{T v_a}{2\pi n Q}. \quad (2)$$

83 In those equations, v_a is the advance velocity; n , rotation rate; D_p , propeller diameter; p_h , hydrostatic pressure;
 84 p_s , saturation pressure; ρ , fluid density; T , thrust force; and Q , torque.

85 The percentage of the propeller suction face covered by cavitation, named p_{cav} , is evaluated by the surface-integral
 86 of volume fraction of the water on the suction face, expressed as:

$$p_{cav} = \frac{\sum_{\Omega_s} \alpha_i A_i}{\sum_{\Omega_s} A_i}, \quad (3)$$

87 in which Ω_s is the suction face of the propeller; α_i , the volume fraction of the vapor; and A_i , the element area.

88 The pressure coefficient C_p is defined as:

$$C_p = \frac{2p}{\rho(nD_p)^2}, \quad (4)$$

89 in which p is the relative pressure.

90 2.2. Validation procedure

91 The validation procedure consists in checking if the numerical model is correctly and accurately predicting the
 92 experimental results, based on an acceptable uncertainty. This work follows the proposed validation method in ASME
 93 (2009), describing the validation uncertainty U_{val} and the validation comparison error E , summarized as:

$$U_{\text{val}}^2 = U_{\text{num}}^2 + U_{\text{exp}}^2 + U_{\text{par}}^2, \quad (5)$$

$$U_{\text{num}}^2 = U_{\text{iter}}^2 + U_{\text{grid}}^2,$$

$$E = S - D, \quad (6)$$

94 in which U_{num} is the numerical uncertainty; U_{par} , parameter uncertainty; U_{exp} , experimental uncertainty; S , numerical
 95 prediction; D , experimental value; and E , comparison error. The numerical uncertainty can be divided in two terms:
 96 iteration uncertainty U_{iter} and discretization uncertainty U_{grid} . In this work, the discretization uncertainty is based on
 97 grid refinement studies (Eça and Hoekstra, 2014); the experimental uncertainty is described in Sec. 4, and the iteration
 98 and parameter uncertainties are assumed to be neglectable compared to the discretization uncertainty.

99 If the comparison error $|E|$ is considerably larger than the validation uncertainty U_{val} , it can be concluded that the
 100 comparison error is dominated by modeling errors, indicating that the adopted numerical model should be improved.
 101 In the case of the comparison error lower than the validation uncertainty, $|E| < U_{\text{val}}$, the modeling error is in between
 102 the noise level, due to the numerical or experimental uncertainties. It can mean two possibilities: if $|E|$ is considered
 103 sufficient small, the numerical error and the experimental solution can be validated, with precision given by U_{val} ;
 104 otherwise, the quality of the numerical solution or the experimental method should be increased before stating any
 105 conclusion about the adequacy of the numerical model.

106 The grid refinement studies based on steady-state simulations are applied in this work because, although the
 107 implicit unsteady model is used, the focus of this study is on the mean value of each output, not on the evolution
 108 of a value over time. Even though the unsteady approach would be recommended, the steady one is adopted for
 109 simplification purposes.

110 2.3. Potential blockage correction

111 Glauert (1983) proposes a one-dimensional potential formulation to correct the effect of tunnel interference when
 112 a propeller is tested. The adopted hypotheses are: the fluid is inviscid and incompressible; any fluid rotation inside
 113 the streamtube is neglected; and the fluid velocity is considered uniform along each cross-section of streamtube.

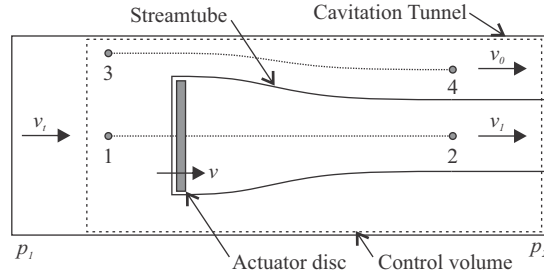


Figure 5: Schema of a propeller inside a cavitation tunnel, under blockage.

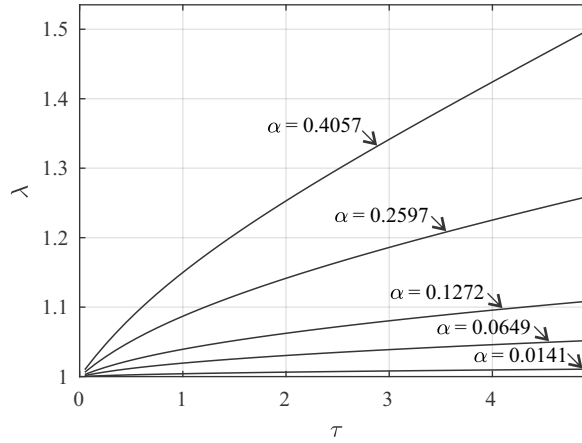


Figure 6: Correlation developed by Glauert (1983) between blockage ratio α , τ and λ , defined in Eq. (7).

114 Figure 5 shows the schematics of the actuator disc model inside a blocked volume, in which v_t represents the tunnel
 115 velocity and v , the velocity inside the actuator disc (in this way, the actuator disc provides an increase of velocity of
 116 $v - v_t$). Due to the confinement, the pressure upstream is not the same as in the downstream, being represented as p_1
 117 and p_2 , respectively.

118 By applying the continuity equation in the control volume, the Bernoulli equation along paths 1-2 and 3-4, and
 119 the momentum equation in the control volume, it is possible to obtain a correlation between the blockage and the
 120 equivalent far-field velocity. Figure 6 summarizes the correction by showing the correlation of λ , the ratio between
 121 the tunnel velocity and the equivalent far-field velocity; and τ , which is proportional to the thrust, being both expressed
 122 in Eq. (7).

$$\alpha = \frac{A_p}{A_t}, \quad \tau = \frac{4J^2 K_T}{\pi}, \quad \lambda = \frac{v_t}{v_\infty}, \quad (7)$$

123 in which α is the blockage ratio; A_p , propeller disc area; A_t , cross sectional area of the slipstream (cross section of the
 124 cavitation tunnel); v_t , tunnel velocity; and v_∞ , equivalent far-field velocity.

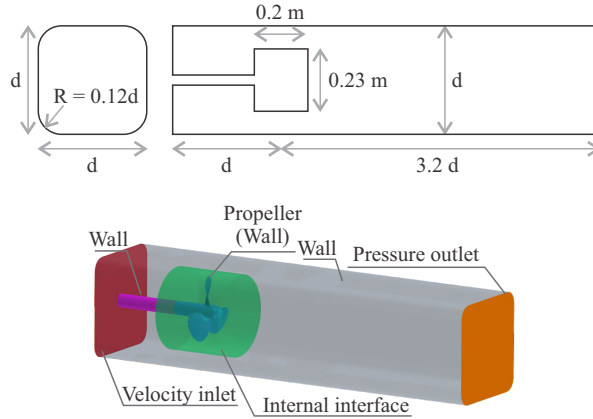


Figure 7: Domain dimensions and boundary conditions of the numerical simulations.

125 3. Numerical approach

126 The numerical simulations are conducted using the CFD software Siemens STAR-CCM+ 13 double-precision.
 127 As detailed in Siemens (2018), the software is based on the cell-centered finite volume method using an unstructured
 128 grid solver. STAR-CCM+ is also used for the mesh generator as for the post-processing.

129 3.1. Domain dimensions and boundary conditions

130 Two numerical regions are used: the rotor region, a cylindrical shape with rotational movement, which contains
 131 the propeller inside; and the stator region, representing the tunnel, with a void space to match the rotor region. Figure 7
 132 shows the dimensions of rotor and stator regions, and the adopted boundary conditions, noting that these two regions
 133 interact through the internal sliding interfaces.

134 The numerical treatment for velocity inlet boundary conditions is that the velocity is specified, the pressure gradi-
 135 ent is zero, and turbulence kinetic energy and specific dissipation rate are also specified. For pressure outlet boundary
 136 condition, velocity gradient is zero, the relative pressure is imposed to be zero, turbulent kinetic energy and specific
 137 dissipation rate gradients are zero.

138 3.2. Physical model and numerical setup

139 Simulations are conducted in an implicit unsteady model, using the unsteady Reynolds-averaged Navier-Stokes
 140 (uRANS) equations with the $k - \omega$ SST turbulence model (Menter, 1994). The Volume of Fluid (VOF) model is
 141 used within the Schnerr-Sauer cavitation model (Sauer and Schnerr, 2001). This cavitation model is based on a
 142 reduced Rayleigh–Plesset equation and neglects the influence of bubble growth acceleration, viscous effects, and
 143 surface tension effects (Siemens, 2018). Segregated flow model is adopted, and the second-order convection is used
 144 in uRANS, SST, and VOF transport equations.

145 Water and vapor are considered incompressible, and its densities are set as 998.16 kg/m^3 and $1.7314 \times 10^{-2} \text{ kg/m}^3$,
 146 respectively; and the dynamic viscosities, $1.0016 \times 10^{-3} \text{ Pa s}$ and $9.7272 \times 10^{-6} \text{ Pa s}$, respectively. Saturation pressure



Figure 8: IPT's Cavitation Tunnel.

147 is set in the temperature of 20 °C, 2339.3 Pa. Turbulence intensity is set to 1%, the same value measured in the IPT's
 148 cavitation tunnel using PIV (Particle Image Velocimetry) in the condition without the propeller. Turbulent length scale
 149 is set as 7% of characteristic length, defined as the chord on the 70% of propeller radius.

150 The Courant number is maintained similar between simulations, defining the timestep as a function of the mean
 151 element size and the velocity, varying between 6.1×10^{-5} s and 9.0×10^{-5} s, compensating its increase in high advance
 152 ratio and high rotation conditions. The volume-average Courant number on the highest timestep is 0.71 in the rotor
 153 region.

154 The simulations ran up to the physical time between 1.21 s and 1.76 s, depending on the monitoring of K_T and
 155 K_Q to achieve a constant value or a constant-oscillatory behavior with a constant mean value. Then, the mean value
 156 of the last 3500 time-steps is assumed as the resulted output.

157 4. Experimental approach

158 Experimental tests are conducted at the IPT's Cavitation Tunnel, shown in Fig. 8. It has a square cross-sectional of
 159 $d = 0.50$ m with a rounded corner. The flow velocity is obtained using a transducer to measure the pressure difference
 160 between two positions of a geometry similar to a Venturi tube. The measurements of thrust and torque are carried out
 161 by two pendulum systems, connecting the drive motor and the load cells. More details of IPT's Cavitation Tunnel can
 162 be found in Dantas et al. (2014).

163 4.1. Uncertainties of the propeller coefficients

164 To obtain the experimental uncertainty of the thrust and torque coefficients, defined in Sec. 2.1, each term that
 165 constitutes these expressions is assumed to be independent. Thus, the propagation of uncertainties is presented below.
 166 Obtaining each of these terms is discussed in further detail in the following sections.

$$\left(\frac{u_{K_T}}{K_T}\right)^2 = \left(\frac{u_T}{T}\right)^2 + \left(\frac{u_\rho}{\rho}\right)^2 + \left(2\frac{u_n}{n}\right)^2 + \left(4\frac{u_{D_p}}{D_p}\right)^2, \quad (8)$$

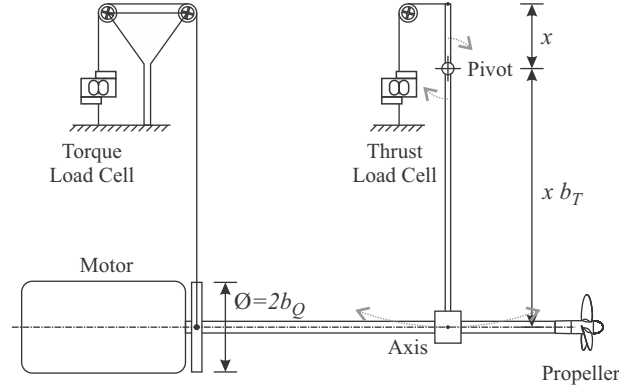


Figure 9: Apparatus of the lever arm used to measure the propeller thrust and torque at IPT's Cavitation Tunnel.

$$\left(\frac{u_{K_Q}}{K_Q}\right)^2 = \left(\frac{u_Q}{Q}\right)^2 + \left(\frac{u_p}{\rho}\right)^2 + \left(2\frac{u_n}{n}\right)^2 + \left(5\frac{u_{D_p}}{D_p}\right)^2. \quad (9)$$

167 4.2. Thrust and torque expressions and uncertainty expansion

168 The load cells are previously calibrated to obtain a linear relation between the voltage and the added mass, given
 169 by $U = \hat{\beta}_0 + \hat{\beta}_1 m$, in which U is the read voltage; m , mass; and $\hat{\beta}$, linear coefficients. The measurement of thrust
 170 starts by reading the thrust load cell voltage, convert to its corresponding mass by using the inverse function of the
 171 one interpolated during calibration, and then convert to force by multiplying with the acceleration of gravity g . Due
 172 to a ratio of forces between the point of measurement of the load cell and propeller thrust, the value is multiplied by
 173 the lever ratio b_T . Figure 9 show the schematics of the Cavitation Tunnel, observing that the lever ratio b_T is the ratio
 174 between the distance of pivot-load cell measurement and the pivot-propeller axis.

175 Torque measurement starts by reading the torque load cell voltage. However, unlike the procedure for thrust, this
 176 value is subtracted by the linearization of the voltage value due to the shaft bearing friction of the cavitation tunnel
 177 axis, using the coefficients $\hat{\beta}_{0,B}$ and $\hat{\beta}_{1,B}$, assuming a linear relation between bearing friction and rotation rate. The
 178 equivalent mass value is multiplied by the acceleration of gravity g , and finally by arm ratio b_Q , resulting in the
 179 propeller torque. Figure 9 also shows schematically the dimension b_Q , which corresponds to the radius of the disc
 180 coupled to the motor.

181 Based on the adopted linear correlations and described procedures, the equations that summarize the thrust T ,
 182 torque Q , and its respective uncertainty propagation u_T and u_Q are expressed by:

$$T = b_T \left(\frac{U_T - \hat{\beta}_{0,T}}{\hat{\beta}_{1,T}} \right) g, \quad (10)$$

$$Q = b_Q \left(\frac{U_Q - \hat{\beta}_{0,Q} - \hat{\beta}_{0,B} - \hat{\beta}_{1,B} n}{\hat{\beta}_{1,Q}} \right) g, \quad (11)$$

$$u_T^2 = \left(\frac{T}{b_T}\right)^2 u_{b_T}^2 + \left(\frac{b_T g}{\hat{\beta}_{1,T}}\right)^2 u_{U_T}^2 + \left(\frac{b_T g}{\hat{\beta}_{1,T}}\right)^2 u_{\hat{\beta}_{0,T}}^2 + \left(\frac{T}{\hat{\beta}_{1,T}}\right)^2 u_{\hat{\beta}_{1,T}}^2 + \left(\frac{T}{g}\right)^2 u_g^2, \quad (12)$$

$$u_Q^2 = \left(\frac{Q}{b_Q}\right)^2 u_{b_Q}^2 + \left(\frac{b_Q g}{\hat{\beta}_{1,Q}}\right)^2 u_{U_Q}^2 + \left(\frac{b_Q g}{\hat{\beta}_{1,Q}}\right)^2 u_{\hat{\beta}_{0,Q}}^2 + \left(\frac{b_Q g}{\hat{\beta}_{1,Q}}\right)^2 u_{\hat{\beta}_{0,B}}^2 + \left(\frac{b_Q g n}{\hat{\beta}_{1,Q}}\right)^2 u_{\hat{\beta}_{1,B}}^2 + \left(\frac{b_Q g \hat{\beta}_{1,B}}{\hat{\beta}_{1,Q}}\right)^2 u_n^2 + \left(\frac{Q}{g}\right)^2 u_g^2 + \left(\frac{Q}{\hat{\beta}_{1,Q}}\right)^2 u_{\hat{\beta}_{1,Q}}^2. \quad (13)$$

183 4.3. Obtaining the uncertainties

184 The uncertainties of thrust and torque load cell voltages are composed by the measurement and resolution uncer-
185 tainties:

$$u_{U_T}^2 = u_{\text{disp},T}^2 + u_{\text{disc},T}^2, \quad u_{U_Q}^2 = u_{\text{disp},Q}^2 + u_{\text{disc},Q}^2. \quad (14)$$

186 The measurement uncertainty u_{disp} is treated as a type-A uncertainty. According to the Vocabulary in Metrology
187 (BiPM et al., 2012) “type-A uncertainty is the evaluation of a component of measurement uncertainty by a statistical
188 analysis of measured quantity values obtained under defined measurement conditions”. It is assumed that the digital
189 data from acquisition systems represent several measurements with a Gaussian distribution, given by $u_{\text{disp}} = s$, in
190 which s is the standard deviation of the sample.

191 To compute the resolution uncertainty u_{disc} , it follows JCGM et al. (2008), which suggests a rectangular distri-
192 bution when using digitally acquired systems, such as load cells and pressure transducers; or triangular distribution,
193 when using analog equipment, usually performed through the eye of a human, such as reading a thermometer or
194 barometer, Eq. (15).

$$u_{\text{disc, rectangular}} = \frac{2a}{\sqrt{12}} = \frac{U_{\text{range}}}{2^{n_{\text{bits}}}} \frac{1}{\sqrt{12}}, \quad u_{\text{disc, triangular}} = \frac{2a}{\sqrt{24}}, \quad (15)$$

195 in which a is the half-width of the interval.

196 The rotation is obtained by a rotary incremental encoder sensor. By performing acquisition through a computer,
197 with high acquisition frequencies, the measurement uncertainty u_{disp} is neglected. Propeller and cavitation tunnel
198 geometry properties, such as diameter and areas, are assumed to have negligible uncertainties.

199 The uncertainties of linear coefficients $u_{\hat{\beta}}$ are given by evaluating the fitting quality during the calibration proce-
200 dure. The water density is determined by the table presented in ITTC (2011b) that correlates these values with the
201 water temperature. Note that the method assumes water with the same properties as in ITTC (2011b). In this way, the
202 uncertainty of method is included, along with the temperature uncertainty.

203 According to the gravimeter data from the Institute of Astronomy, Geophysics and Atmospheric Sciences (IAG)
204 of the University of São Paulo, the measured gravity is $g = 9.7864(3) \text{ m/s}^2$. The value and its uncertainty are used for
205 subsequent calculations, as the IAG is located less than 500 m from the Cavitation Tunnel.

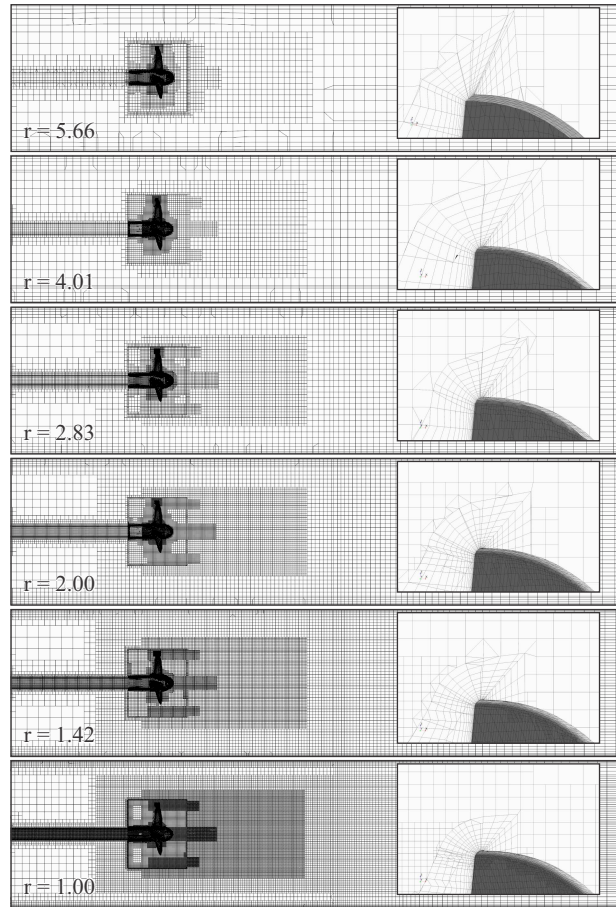


Figure 10: Mesh topology and detail of the P104 tip, from the most coarse (top) to finest mesh (bottom).

206 5. Results

207 5.1. Verification and Validation with experimental results

208 The Verification and Validation (V&V) is conducted to validate the numerical part with the experimental results.
 209 To do so, the propeller P104 is studied only in the same blockage ratio of the experimental facility. The numerical
 210 uncertainties are estimated based on the grid refinement studies (Eça and Hoekstra, 2014), adopting five meshes with
 211 similar topologies and different refinements. Figure 10 shows the adopted meshes, with similar hexahedral topologies,
 212 and the detail on the propeller mesh tip, showing the prism layer used to accurately model the boundary layer and the
 213 tip vortex detachment. Table 1 shows key characteristics of the grids.

214 The V&V procedure is carried out in four conditions: from low advance ratio ($J = 0.25$, a condition with sig-
 215 nificant cavitation) to the advance ratio close to the maximum hydrodynamic efficiency ($J = 0.71$). All cases have a
 216 Reynolds number of $Re_p = 1.06 \times 10^6$ and cavitation index of $\sigma = 2.30$. Figure 11 presents the results for each case
 217 over each mesh level, along with its numerical and experimental results and their respective uncertainties.

Table 1: Number of elements N_e in each region; characteristic length h (average blade near-wall cell size); and cell size ratio $r = h/h_{\text{finest}}$.

Stator N_e	Rotor N_e	Total N_e	h [10^{-3} mm]	r
2.7 M	6.8 M	9.5 M	2.357	1.00
1.0 M	4.7 M	5.7 M	3.348	1.42
478 k	3.5 M	4.0 M	4.714	2.00
232 k	3.1 M	3.3 M	6.663	2.83
254 k	1.9 M	2.2 M	9.449	4.01
97 k	1.5 M	1.6 M	13.33	5.66

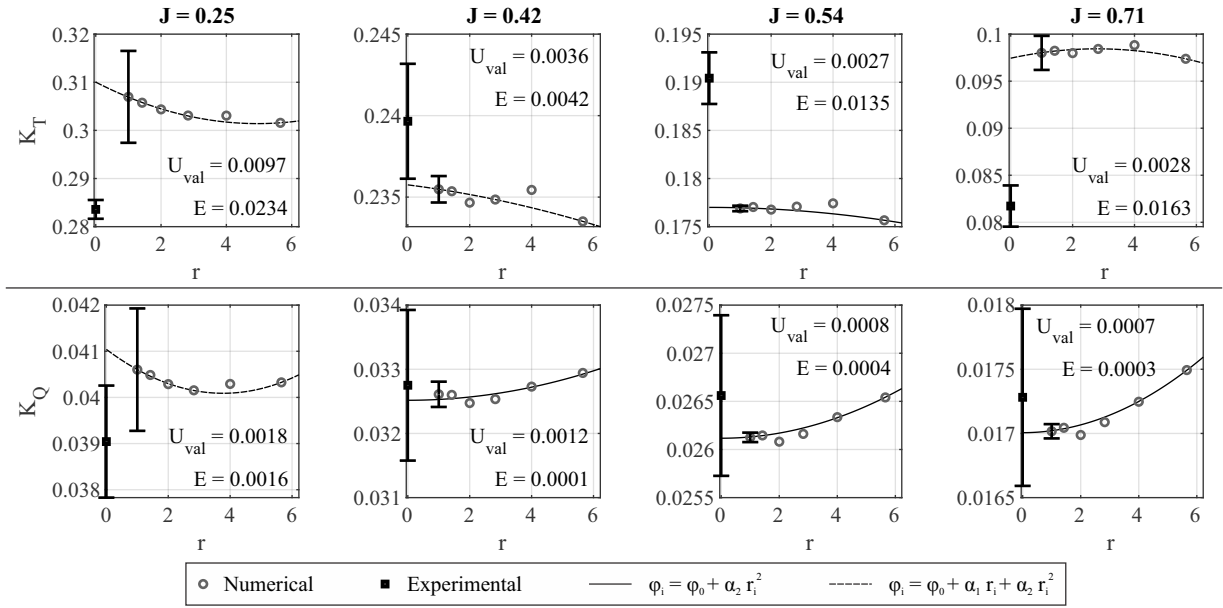


Figure 11: Comparison between numerical results from each cell size ratio r (circle markers), the experimental results (square marker at $r = 0$), and the curve to estimate the discretization error.

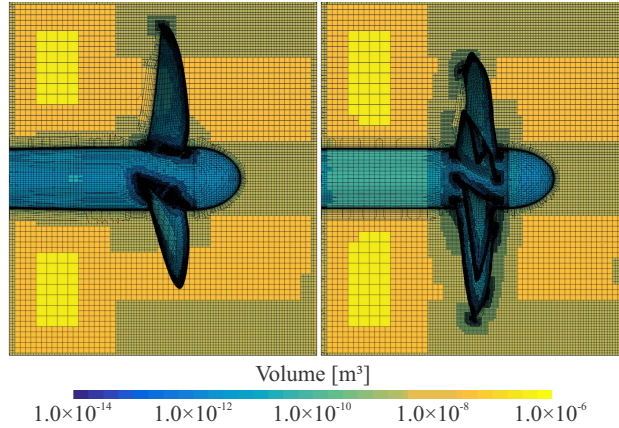


Figure 12: Adopted rotor meshes for the P104 (left, rotor $N_e = 6.8$ M) and P107 (right, rotor $N_e = 11.2$ M) propellers.

218 The analyses show that most of the numerical results are in the range of the validation uncertainty U_{val} , making it
 219 validated with their respective uncertainties. Larger values of uncertainties in the experimental torque coefficients K_Q
 220 are related to the shaft bearings friction uncertainties. Some of the results have shown that the comparison errors E
 221 are in the same order of magnitude of validation uncertainties U_{val} . The comparison errors for most of the presented
 222 cases indicate that the model errors are below the noise levels, suggesting that the numerical model can be considered
 223 valid for a comparative analysis of the blockage effect. Most of the order of convergence for K_Q ($J = 0.42, 0.54, 0.71$)
 224 have an observed grid convergence of $p = 2.0$ ($\phi_i = \phi_0 + \alpha_2 r^2$), indicating a monotonically converging solution.
 225 On the other hand, K_T results have mostly non-monotonic convergence ($J = 0.25, 0.42, 0.71$), with equation of
 226 $\phi_i = \phi_0 + \alpha_1 r + \alpha_2 r^2$ (Eça and Hoekstra (2014) describes that these types of equations are made as a shortcoming of
 227 “practical calculations”). Also, the discretization uncertainty U_{grid} compared to the result from the most refined mesh
 228 ϕ_1 is higher for the condition of low advance ratio ($U_{\text{grid}}/\phi_1 = 3.1\%$ for the K_T and $U_{\text{grid}}/\phi_1 = 3.3\%$ for the K_Q).
 229 Due to significant cavitation, it suggests that a finer mesh or further improvements of the numerical model could be
 230 addressed to enhance the quality of numerical results.

231 Moreover, it is important to point out that parameter uncertainty is not considered in this validation procedure. Due
 232 to the inherent characteristics of the IPT’s Cavitation Tunnel, the measurement of the advance velocity by the Venturi
 233 effect is affected by the propeller load, interfering in the uncertainty of the advance ratio. During the experimental
 234 tests, uncertainty on the advance velocity was observed, implying that the experiments may present some uncertainty
 235 in reproducing the same condition as simulated in the CFD. Nonetheless, it still suggests that the chosen numerical
 236 model is satisfactory to proceed to the next part of the comparative analysis to assess the blockage effect. The same
 237 mesh topology and refinements of the $r = 1.0$ mesh are applied on the P107 rotor mesh. Figure 12 shows the adopted
 238 meshes for the P104 and P107 propellers, demonstrating their density similarities.

Table 2: Dimensions of the numerical cavitation tunnel d (see Fig. 7), cross sectional area A_t , and the blockage ratio α .

d [m]	A_t [m ²]	α (P104)	α (P107)
0.28	0.077	0.4057	0.3623
0.35	0.121	0.2597	0.2319
0.50	0.247	0.1272	0.1136
0.70	0.484	0.0649	0.0580
1.50	2.222	0.0141	0.0126

Table 3: Test cases descriptions.

Test case	Propeller	Re_p	σ
1	P104	9.97×10^5	3.1
2	P104	1.40×10^6	1.0
3	P107	9.97×10^5	3.1

239 5.2. Comparison with experimental results

240 Based on the numerical method, validated in the last subsection, the propeller performance coefficients are ob-
 241 tained from numerical and experimental approaches. The propeller P104 is tested and compared with the numerical
 242 results using the same blockage ratio of the IPT's Cavitation Tunnel. Two sets of simulations are conducted, varying
 243 the cavitation number and the hydrostatic pressure. The first set presents $Re_p = 9.97 \times 10^5$ and $\sigma = 3.1$, whereas the
 244 other one, $Re_p = 1.40 \times 10^6$ and $\sigma = 1.0$. Figure 13 illustrates the results of these two sets for $\alpha = 0.1272$, showing
 245 the K_T , K_Q , and η_0 curves along with J . Furthermore, the cavitation pattern, represented by the iso-surface of 0.5
 246 volume fraction of water, is shown in the K_T plot. Due to blade view, hub vortex cavitation cannot be seen, although
 247 it is also simulated.

248 For low values of J , both conditions of σ imply some level of cavitation, but the $\sigma = 1.0$ case results in cavitation
 249 intense enough to decrease the K_T for low advance ratio, due to the suction face mostly covered by cavitation. This
 250 behavior is observed in both numerical and experimental results, which ensures the quality of the adopted numerical
 251 model when compared with experimental tests.

252 5.3. Blockage effects on the propeller performance coefficients

253 The blockage effect is analyzed by changing the cross-section size of the numerical cavitation tunnel. Five different
 254 tunnel cross-section sizes, described in Tab. 2, are evaluated with their respective meshes, shown in Fig. 14.

255 To analyze the blockage effects on the propeller performance coefficients, three cases are tested, described in
 256 Tab. 3.

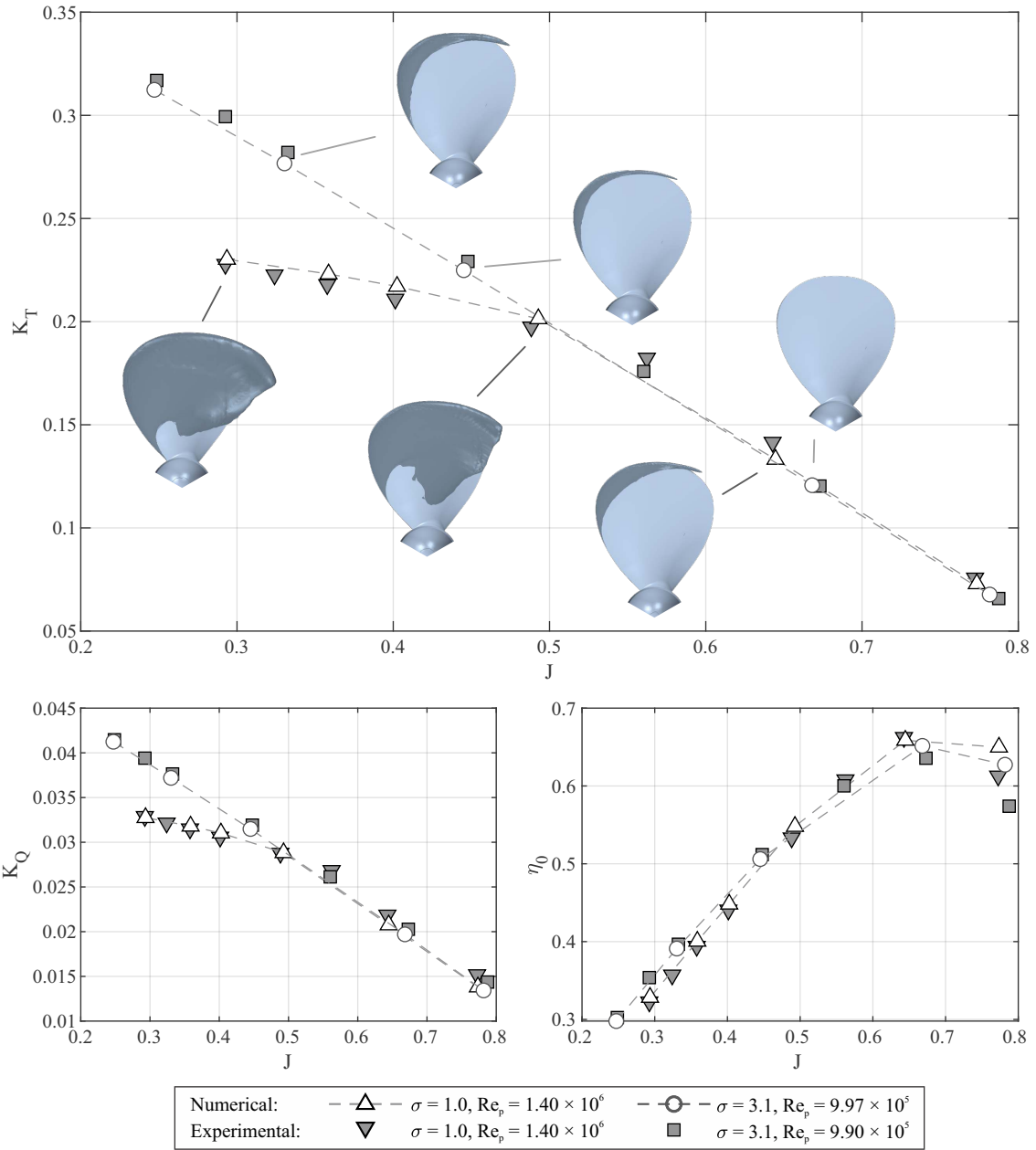


Figure 13: Numerical and experimental results of P104 thrust, torque and hydrodynamic efficiency versus advance ratio J for blockage ratio of $\alpha = 0.1272$. Cavitation pattern of numerical results (iso-surface of 0.5 volume fraction of water) for cavitation indices of $\sigma = 3.1$ and $\sigma = 1.0$.

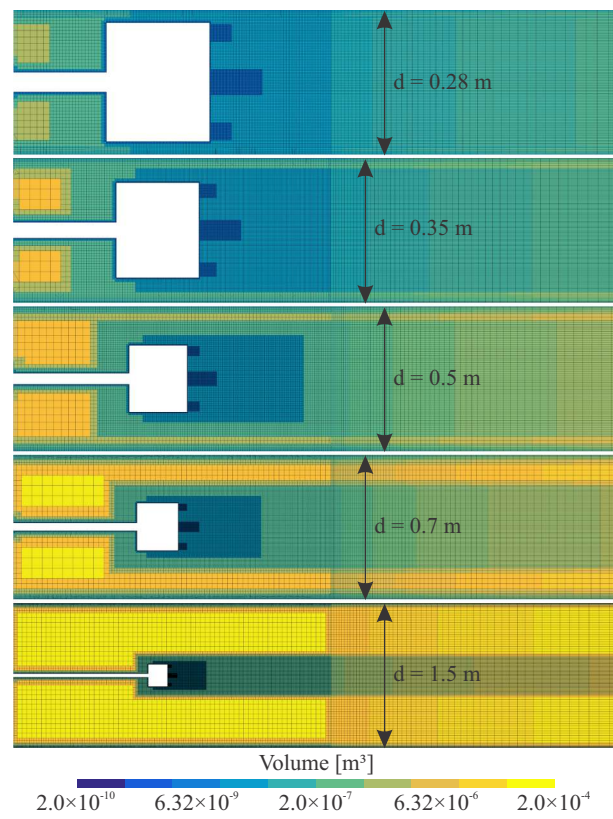


Figure 14: Adopted stator meshes from $d = 0.28 \text{ m}$ (top) to $d = 1.5 \text{ m}$ (bottom). The space void to match with the rotor region has the same dimension in all stator meshes.

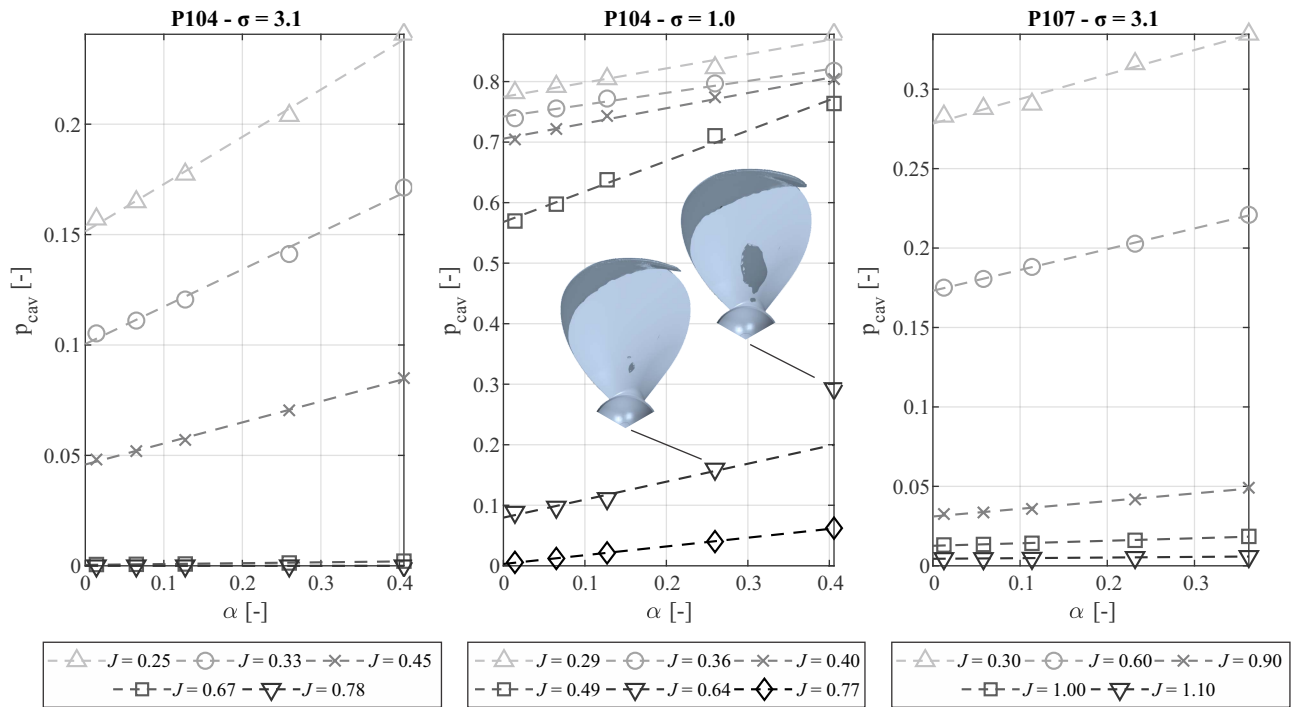


Figure 15: Percentage of suction face covered by cavitation p_{cav} versus blockage ratio α .

257 Figure 15 shows the percentage of the suction face covered by cavitation p_{cav} along with the blockage ratio, for
 258 several conditions of advance ratio. The changing of values depending on the blockage ratio confirms a dependence
 259 between the blockage ratio and cavitation pattern. Linear regression is also plotted, suggesting a linear relationship
 260 between the blockage ratio and the p_{cav} . The condition of test case 2 at $J = 0.64$ and $\alpha = 0.4057$ seems to be an outlier,
 261 being ignored in the proposed linear fit. Figure 15 also shows the cavitation pattern comparison of this condition and
 262 in a lower blockage ratio. Considerable cavitation in the central region is notable only in the higher blockage condition
 263 being related to the over-increase of p_{cav} .

264 These linear regressions can be extrapolated to obtain the expected values of p_{cav} for $\alpha = 0.0$, a no-blockage
 265 condition. Analyzing the test case 1 at $J = 0.25$, it shows a p_{cav} difference of 2.8% between the expected value for
 266 $\alpha = 0.0$ and $\alpha = 0.1272$; whereas for test case 2 at $J = 0.49$, it presents a difference of 6.9%. For the test case 3 at
 267 $J = 0.60$, a difference of 1.5% is obtained between the expected value of $\alpha = 0.0$ and $\alpha = 0.1136$.

268 Figure 16 and Fig. 17 show the propeller P104 performance coefficients, including the p_{cav} , at $\sigma = 3.1$ and
 269 $\sigma = 1.0$, respectively (test case 1 and 2); and Fig. 18, the propeller P107 performance coefficients at $\sigma = 3.1$ (test
 270 case 3). The left-hand side of the following figures present the obtained results, and on the right-hand side, blockage
 271 corrected based on the method described in Sec. 2.3.

272 The left-hand side of Fig. 16 shows that thrust and torque increase as the blockage increases in all simulated
 273 advance ratios. Applying the blockage correction by adjusting the advance ratio, the variables K_T , K_Q , and η_0 on

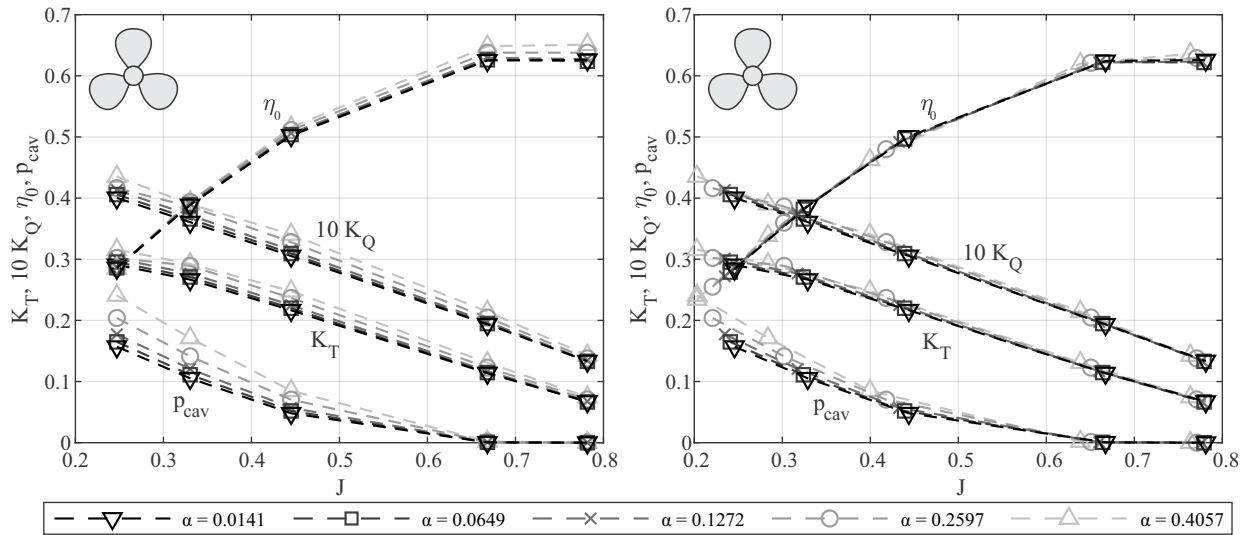


Figure 16: Propeller P104 at $\sigma = 3.1$ (test case 1): propeller performance diagram with advance ratio, original results (left), and with blockage correction (right).

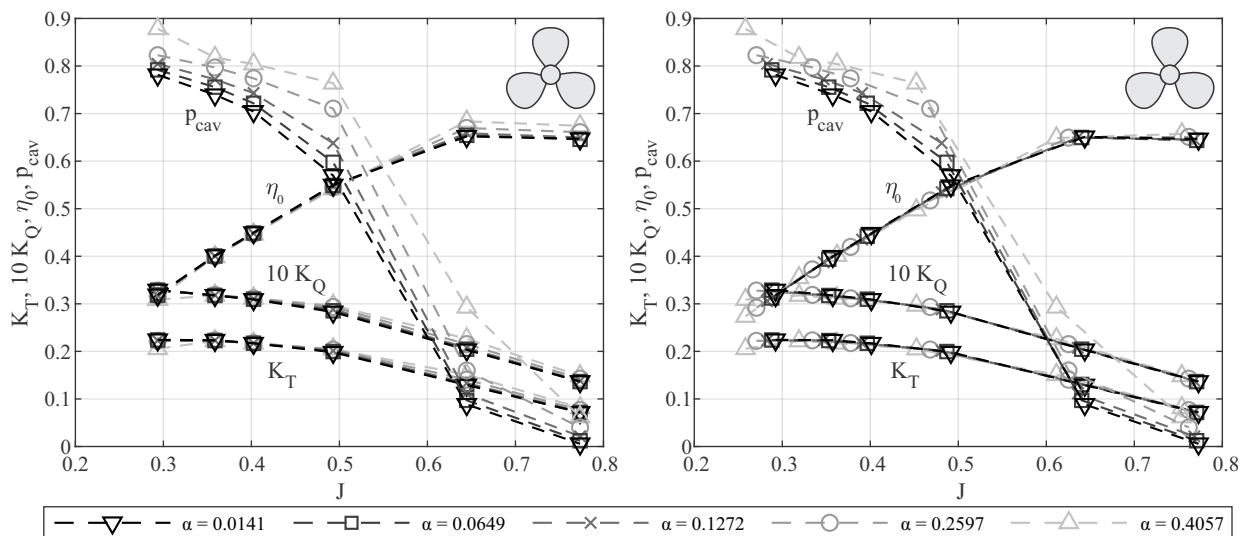


Figure 17: Propeller P104 at $\sigma = 1.0$ (test case 2): propeller performance diagram with advance ratio, original results (left), and with blockage correction (right).

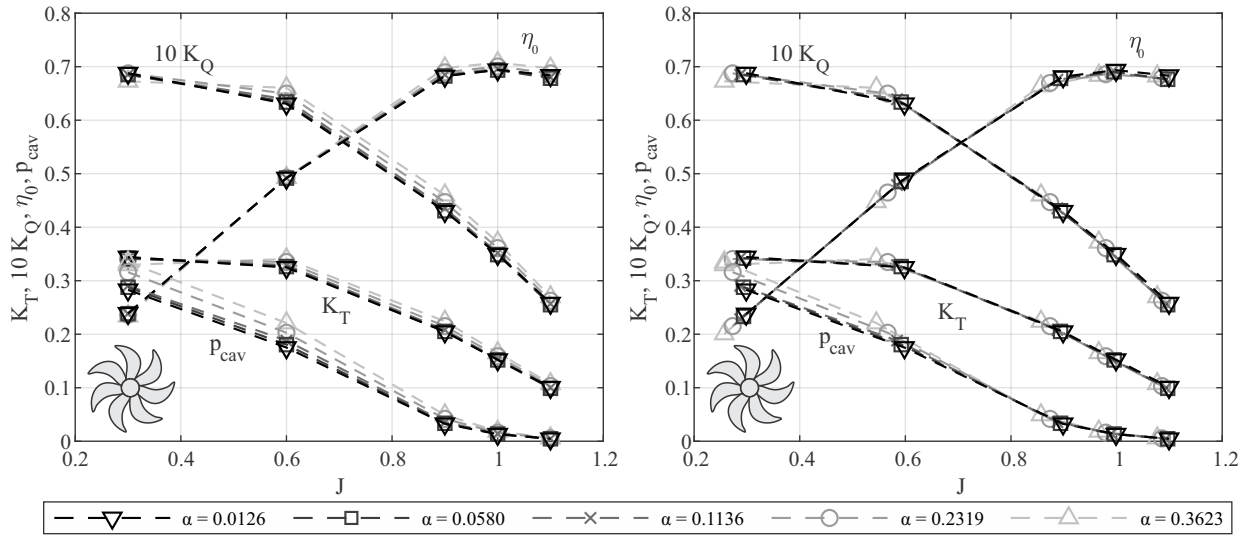


Figure 18: Propeller P107 at $\sigma = 3.1$ (test case 3): propeller performance diagram with advance ratio, original results (left), and with blockage correction (right).

274 the right-hand side of Fig. 16 seem to converge to the same curve, showing high blockage curves getting closer
 275 to low blockage ones after the correction, suggesting a convergence of curves for different blockages. Although
 276 Glauert stated that the correction may be unreliable for low values of the advance ratio because the conventional
 277 type of slipstream assumed in the theory no longer occurs, for this presented case, the correction is satisfactory in
 278 all conditions. The correction on the p_{cav} does not present the same level of convergence as which is observable for
 279 other propeller performance coefficients. Although the suction face is 24% covered by cavitation, it is not enough
 280 to considerably change the linear shape of K_T and K_Q curves along with the J values. Hence, the Glauert blockage
 281 correction seems to perform a good correction for the propeller performance indicators, even when the suction face is
 282 24% covered by cavitation, but the p_{cav} corrected is not as good as which observed in the main propeller performance
 283 coefficients.

284 The propeller performance diagram of the second test case, P104 at $\sigma = 1.0$, is shown in Fig. 17. Different from
 285 the previous case, for the lowest advance ratio, $J = 0.29$, the higher the blockage is not followed by higher values of
 286 K_T and K_Q . Also, K_T and K_Q curves are not as linear for low values of J as it is previously observed for $\sigma = 3.1$
 287 case. The third test case, P107 at $\sigma = 3.1$, Fig. 18, follows the same behavior as observed in the second test case:
 288 for the lowest advance ratio, $J = 0.30$, the higher the blockage is also not followed by higher values of K_T and K_Q .
 289 Indeed, the right-hand side plot shows that the blockage correction converges the different conditions of blockage to
 290 the same curve for values higher than $J = 0.6$. The blockage effect typically increases the thrust, which is mainly
 291 a consequence of an increased pressure difference between suction and pressure faces. In these extreme cases of
 292 considerable cavitation, observed in test cases 2 and 3, the blockage pushes down the suction pressure, and being
 293 limited by cavitation, limits the thrust. Section 5.4 studies this phenomenon in details.

294 Furthermore, in all cases, the correction seems to not converge correctly the p_{cav} , at least not as good as observable
 295 in the propeller performance coefficients. However, it is important to emphasize that extreme cases of cavitation
 296 are not usual for practical conditions, thus being a rare condition to be tested on a cavitation tunnel. Therefore,
 297 Glauert presented a good approach to correct the blockage effect for the propeller performance coefficients even when
 298 cavitation is moderate.

299 5.4. Blockage effects on the pressure distribution

300 A further investigation is made to assess the combination of phenomena between the increase of thrust due to
 301 blockage effect and decrease, due to cavitation. Five conditions are analyzed: high load conditions of P104 (at
 302 $\sigma = 3.1$ and $\sigma = 1.0$) and P107; and close to the maximum efficiency condition of P104 (at $\sigma = 3.1$) and P107. In
 303 the following figures, it is presented the thrust coefficient from the suction and pressure faces and from the hub, called
 304 $K_{T,s}$, $K_{T,p}$, and $K_{T,h}$, respectively. The total thrust coefficient contribution is such that $K_T = K_{T,p} + K_{T,s} + K_{T,h}$. In
 305 addition, the level curves of the pressure coefficient C_p at the lowest and highest blockage ratios are presented. Note
 306 that in suction face figures, negative value of pressure coefficients contribute to the increase of total K_T .

307 To analyze the propellers close to the maximum efficiency point, Fig. 19 presents the results of the test case 1 (P104
 308 at $\sigma = 3.1$) at $J = 0.66$; and Fig. 20, test case 3 (P107) at $J = 1.0$. In these conditions, the presence of cavitation
 309 is small. As observed in Fig. 16, when the cavitation is not predominant, the higher the blockage ratio the higher is
 310 the thrust coefficient. However, results show that these increases of thrust due to blockage are observed only on the
 311 suction face. The pressure face and hub demonstrate a different behavior: decreasing the $K_{T,p}$ and $K_{T,h}$ as the blockage
 312 gets higher. A look into the the P104 case shows that proportionally the suction face contribution is $K_{T,s}/K_T = 89\%$,
 313 comparing to the $K_{T,p}/K_T = 14\%$ for the pressure face and $K_{T,h}/K_T = -3\%$ for the hub (for $\alpha = 0.4057$). For the P107
 314 case, the contribution is 143% from the suction face; -41%, pressure face; and -2%, hub (for $\alpha = 0.3623$). Hence,
 315 even though the $K_{T,p}$ and $K_{T,h}$ decrease as the blockage ratio increases, it is proportionally less influential than the
 316 increase of $K_{T,s}$. The C_p distribution on the suction face for both P104 and P107 propellers demonstrates a decrease
 317 of pressure on the central region of the blade, which is the largest region of the blade that contributes to the thrust. On
 318 the other side, the pressure face shows a decrease of level curve size of $C_p = 0.125$, which contributes to the decrease
 319 of the thrust.

320 A condition with more cavitation is studied in Fig. 21: test case 1 (P104 at $\sigma = 3.1$) at $J = 0.24$, a high-load
 321 condition. The behavior observed in the last analysis still stands: as the blockage ratio increases, the thrust on the
 322 suction side increases, and decreases on the pressure side and hub. In this case, there is a considerable portion of
 323 cavitation, which can be observed by the dark blue area on the suction face, indicating regions with C_p lower than
 324 -2.0 , being limited by cavitation. It is possible to observe a decrease of C_p in the central region of the suction face.
 325 Also, on the pressure side, higher values of C_p decrease and move to the left part (leading edge) of the propeller. The
 326 pressure distribution on the hub shows also that the $C_p = -0.625$ curve enlarged as the blockage increased, explaining
 327 the $K_{T,h}$ reduction.

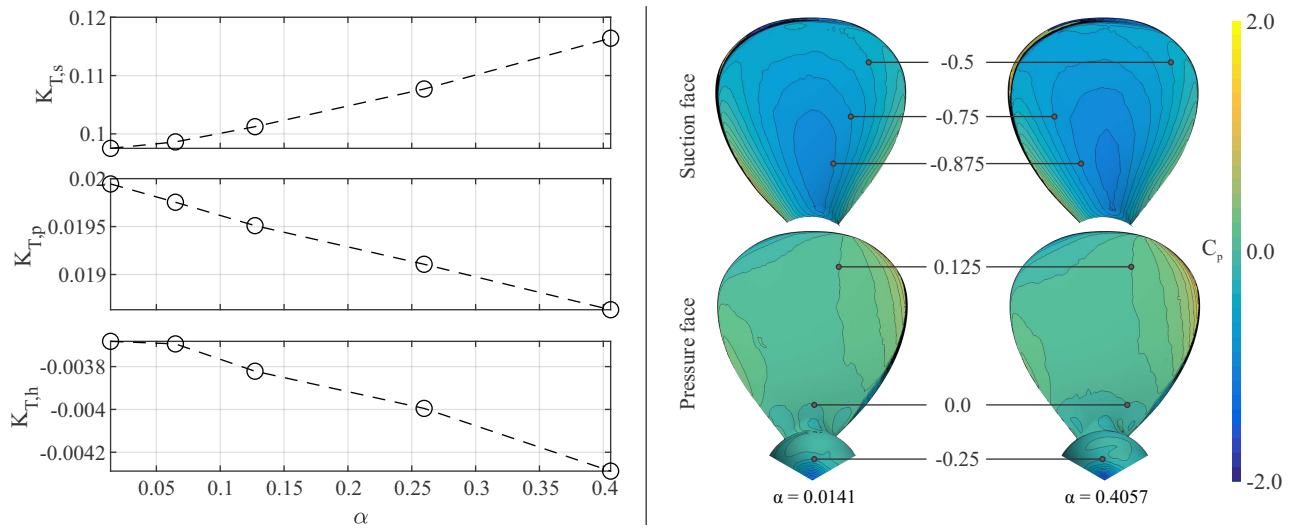


Figure 19: Propeller P104 at $\sigma = 3.1$ and $J = 0.66$: thrust coefficient from the suction ($K_{T,s}$), pressure ($K_{T,p}$), and hub ($K_{T,h}$) surfaces; and the pressure coefficient C_p distribution of the lowest and highest blockage ratio.

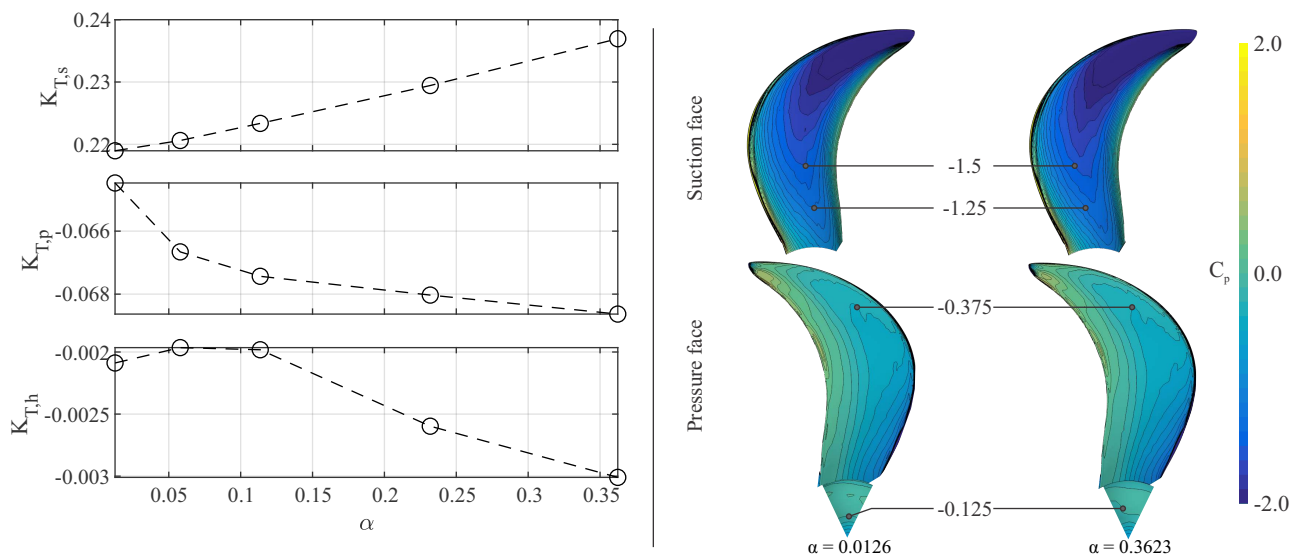


Figure 20: Propeller P107 at $\sigma = 3.1$ and $J = 1.00$: thrust coefficient from the suction ($K_{T,s}$), pressure ($K_{T,p}$), and hub ($K_{T,h}$) surfaces; and the pressure coefficient C_p distribution of the lowest and highest blockage ratio.

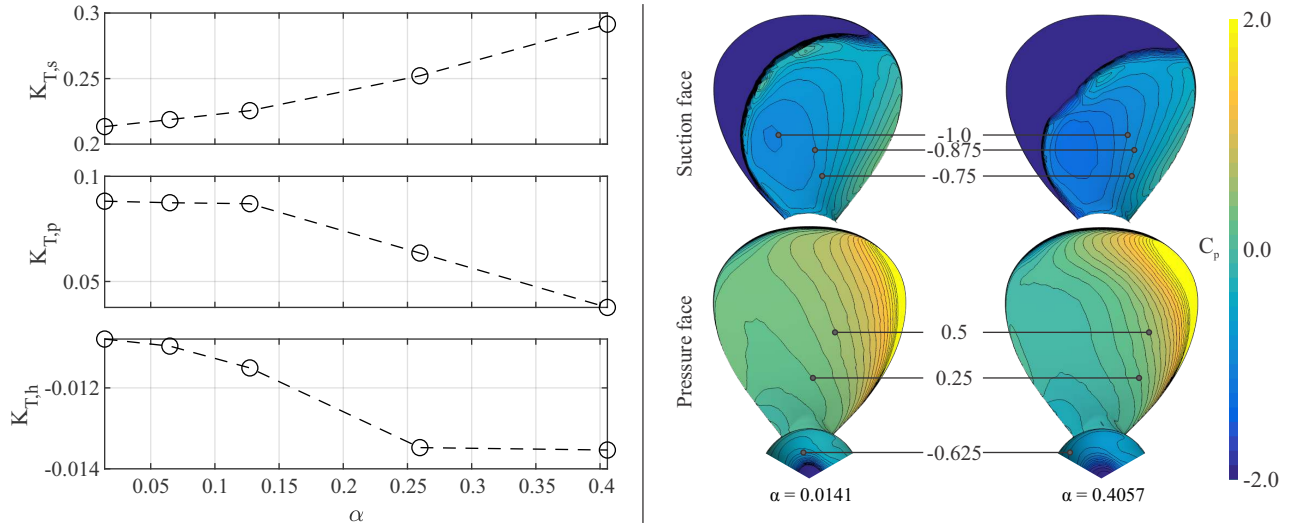


Figure 21: Propeller P104 at $\sigma = 3.1$ and $J = 0.24$: thrust coefficient from the suction ($K_{T,s}$), pressure ($K_{T,p}$), and hub ($K_{T,h}$) surfaces; and the pressure coefficient C_p distribution of the lowest and highest blockage ratio.

328 The extreme case of each propeller, which thrust decreases as the blockage increases, is analyzed: test case 2
 329 (P104 at $\sigma = 1.0$) at $J = 0.29$; and test case 3 (P107) at $J = 0.30$. Figure 22 and Fig. 23 show its respectively analysis.
 330 Although the observed decrease of K_T with blockage, the behavior of the higher the blockage ratio, the higher is the
 331 $K_{T,s}$ and the lower are $K_{T,p}$ and $K_{T,h}$ still maintains in both cases. Indeed, observing the C_p distribution, it is noted that
 332 a considerable area is covered by cavitation. For the P104 case, the level curve $C_p = -1.0$ is more present close to the
 333 axis, increasing the thrust from the suction face. On the other hand, the pressure face distribution has a considerable
 334 decrease of $C_p = 0.25$ and $C_p = 0.125$ due to the blockage. Figure 19 and Fig. 21 have shown that the central region
 335 of the blade is the most contributor to the propeller on the suction face. As in these cases most of the central region is
 336 covered by cavitation, limiting the minimal pressure, the increase of $K_{T,s}$ due to the blockage is less intense.

337 The difference between the highest and the lowest simulated blockage ratio of P104 case (Fig. 22) results in
 338 $\Delta K_{T,s} = 0.007$, $\Delta K_{T,p} = -0.0241$, and $\Delta K_{T,h} = -0.0018$. Therefore, the decrease of total K_T can be mainly attributed
 339 to the pressure side contribution, as $\Delta K_{T,p}$ is 13 times higher than $\Delta K_{T,h}$. Thus, the decreasing of $K_{T,p}$ being more
 340 intense than the increase of $K_{T,s}$ explains the phenomenon of the decrease of K_T with the blockage.

341 For the propeller P107, Fig. 23 shows a reverse on the signal of $K_{T,p}$, being positive for $\alpha = 0.1136$, and negative
 342 for higher blockages. Indeed, observing the C_p distribution, it is noted a growing of level curve $C_p = -0.375$ on the
 343 center of the blade. Furthermore, the level curve $C_p = -0.75$ also increases in the center of hub, decreasing the $K_{T,h}$
 344 with the blockage ratio. The difference of thrust coefficients between the highest and lowest blockage ratio results
 345 in $\Delta K_{T,s} = 0.0362$, $\Delta K_{T,p} = -0.0464$, and $\Delta K_{T,h} = -0.0044$. Again, being $\Delta K_{T,p}$ approximately 11 times larger than
 346 $\Delta K_{T,h}$, it can be attributed the decrease of $K_{T,p}$, along with the moderate increase of $K_{T,s}$, as the main cause of thrust
 347 decrease with the blockage ratio.

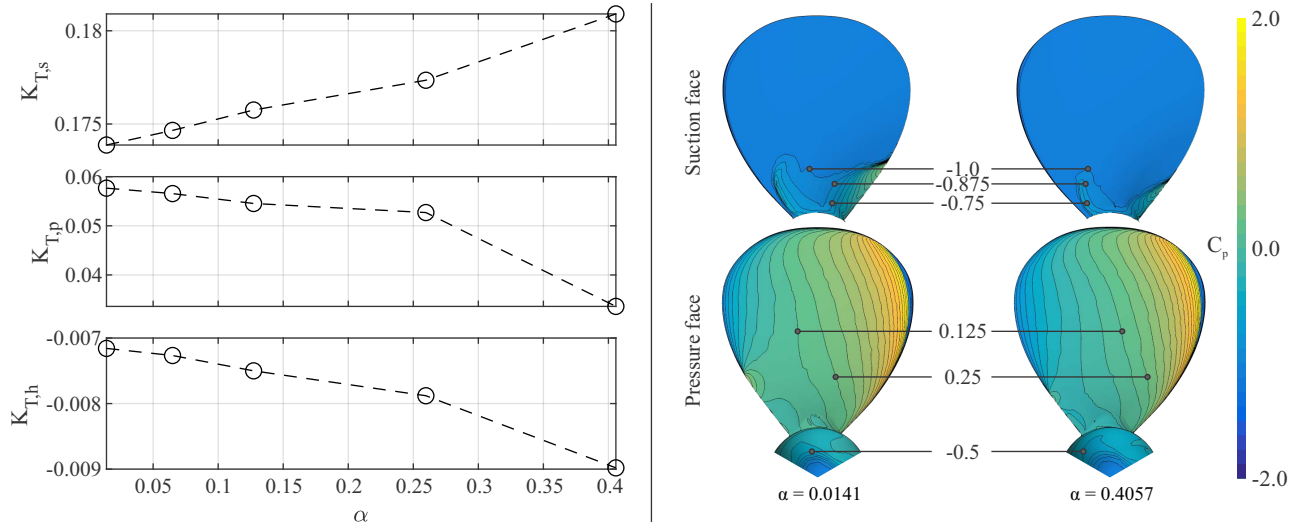


Figure 22: Propeller P104 at $\sigma = 1.0$ and $J = 0.29$: thrust coefficient from the suction ($K_{T,s}$), pressure ($K_{T,p}$), and hub ($K_{T,h}$) surfaces; and the pressure coefficient C_p distribution of the lowest and highest blockage ratio.

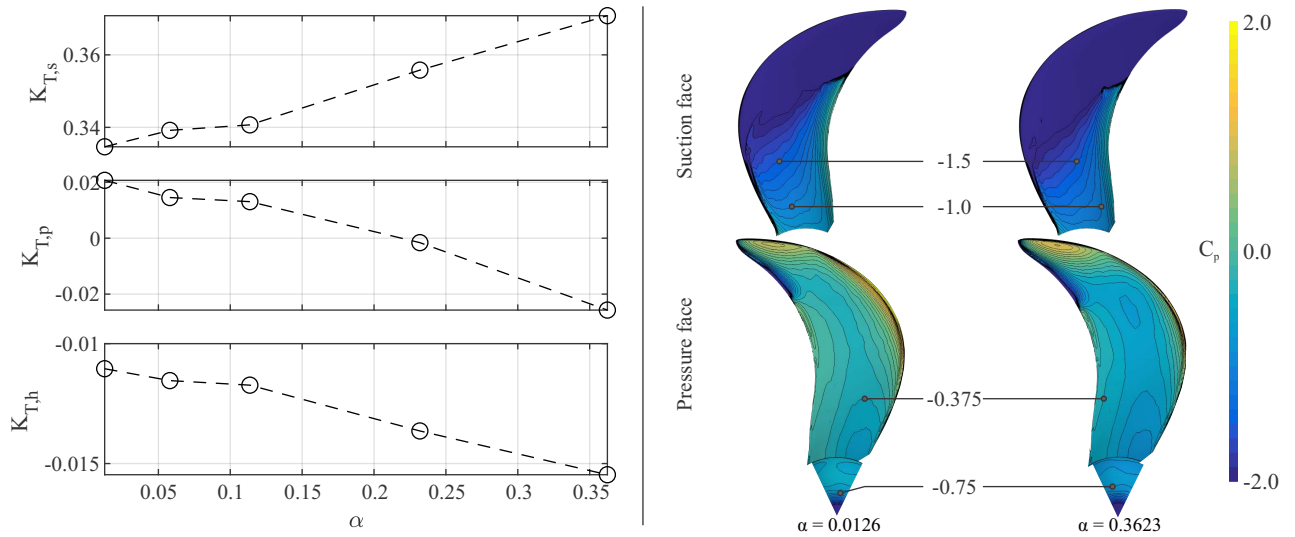


Figure 23: Propeller P107 at $\sigma = 3.1$ and $J = 0.30$: thrust coefficient from the suction ($K_{T,s}$), pressure ($K_{T,p}$), and hub ($K_{T,h}$) surfaces; and the pressure coefficient C_p distribution of the lowest and highest blockage ratio.

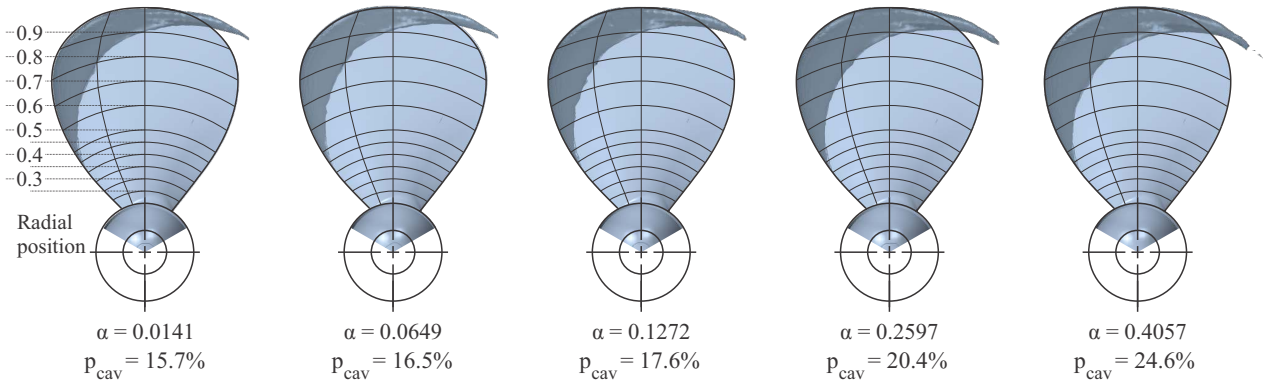


Figure 24: Propeller P104 at $\sigma = 3.1$ and $J = 0.24$: comparison of the cavitation pattern (iso-surface of water volume fraction of 0.5).

348 In all observed cases, a general observation that can be made is that the thrust from the suction face increases
 349 as the blockage ratio increases; and from the pressure face and the hub, decreases as the blockage ratio increases.
 350 The adopted conventional hub geometry resulted in a negative $K_{T,h}$ in all observed cases, reducing the total thrust
 351 coefficient. However, comparing the influence of $K_{T,h}$ and $K_{T,p}$ to the total thrust, it is observed that the thrust
 352 reduction due to blockage effects is higher from the pressure side than from the hub. When cavitation is predominant,
 353 the suction face has a limited increase of thrust due to blockage. In extreme conditions, the decrease of thrust from
 354 the pressure side overcomes the increase of $K_{T,s}$, leading to a decrease of total thrust as blockage gets higher. As the
 355 suction face is being limited by the cavitation, it is not recommended to apply the blockage correction in such intense
 356 cavitation conditions, as the correction does not predict this limitation of the minimal pressure.

357 5.5. Blockage effects on the cavitation pattern

358 A closer look is done to analyze the cavitation pattern for the high-load conditions. For the first test case (P104 at
 359 $\sigma = 3.1$), Fig. 24 shows the cavitation pattern at $J = 0.24$, in which it is possible to qualitatively observe the effect
 360 of the blockage effect. For example, taking a close look at the radial position of 0.8 and $\alpha = 0.0141$, it is possible to
 361 observe that the cavitation surface, represented by the VOF iso-surface of 0.5, ends on the quarter-chord line. Indeed,
 362 this pattern is closely maintained up to the intermediate blockages, up to $\alpha = 0.1272$. For higher blockages and still on
 363 the radial position of 0.8, the cavitation pattern ends after the quarter-chord. Thus, although it is possible to observe
 364 an influence of the blockage, the qualitative results suggest that the blockage of $\alpha = 0.1272$ has a small difference
 365 when compared to the lowest blockage.

366 The same analysis is done for the second test case (P104 at $\sigma = 1.0$ case): Fig. 25 shows the cavitation pattern
 367 on the suction side at $J = 0.29$. For the $\alpha = 0.4057$, cavitation covers most of the region close to the axis, reaching a
 368 radial position of 0.25 in the middle of the blade; whereas, for $\alpha = 0.0141$, it reaches a radial position of 0.35.

369 For the third test case (P107 at $\sigma = 3.1$), Fig. 26 shows the cavitation pattern on the suction side at $J = 0.30$.
 370 Observe that for the lowest blockage, the cavitation starts at the radial position of 0.7 on the blade reference line,

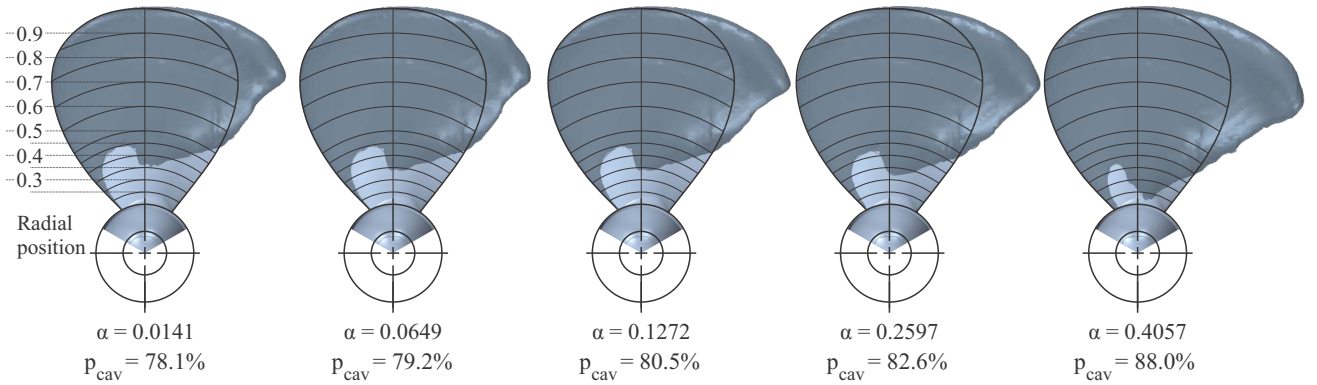


Figure 25: Propeller P104 at $\sigma = 1.0$ and $J = 0.29$: comparison of the cavitation pattern (iso-surface of water volume fraction of 0.5).

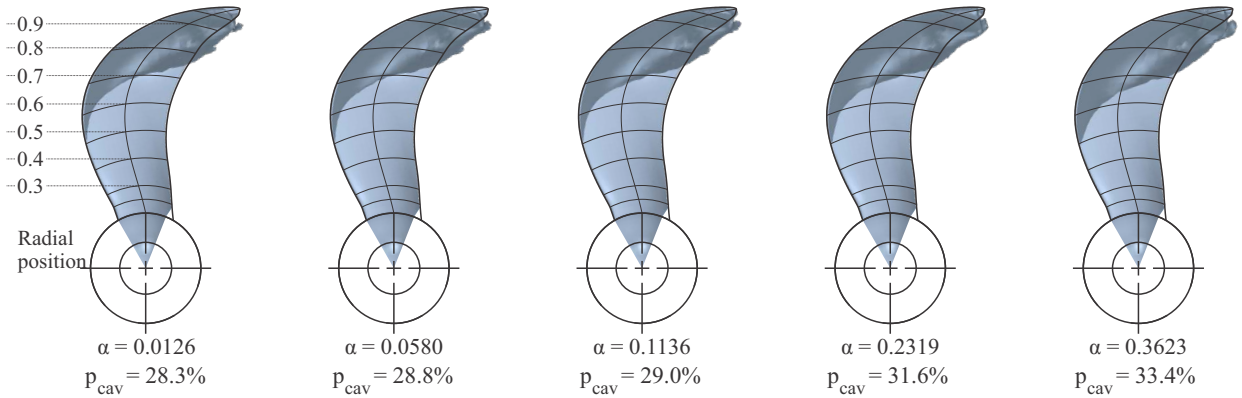


Figure 26: Propeller P107 at $\sigma = 3.1$ and $J = 0.30$: comparison of the cavitation pattern (iso-surface of water volume fraction of 0.5).

371 whereas for the highest blockage, the cavitation starts at 0.65. The behavior observed with P107 is similar to the
 372 previous cases, reassuring the dependence of the cavitation pattern and blockage.

373 Although p_{cav} is sensitive to blockage, based on the qualitative results of the first and second test cases, the
 374 comparison of the lowest blockage ratio with the same found in the IPT's cavitation tunnel ($\alpha = 0.1272$) shows that
 375 the pattern is similar. For the third test case, the results show a similarity of the cavitation pattern of $\alpha = 0.0126$ to
 376 0.1136 , also represented by the small change on the p_{cav} .

377 In summary, based on these three test cases, it is possible to assume that the cavitation pattern is indeed affected by
 378 the blockage ratio. The IPT's Cavitation Tunnel blockage seems to be appropriate to observe the cavitation pattern and
 379 the ITTC recommendation of a blockage ratio no higher than 20% (ITTC, 2016) is, based on the analyzed propellers,
 380 the maximum blockage ratio that can be suggested in the experiments to study cavitation patterns.

6. Conclusions

This work studied the blockage effect influence on a marine propeller using CFD tools by analyzing the thrust, torque, hydrodynamic efficiency, and cavitation area. The adopted physical models were validated with experimental tests from IPT's Cavitation Tunnel, in conditions that present the cavitation phenomena. To ensure that the adopted numerical model is appropriate, the experimental uncertainties were composed and compared with the numerical uncertainty. Then, the work was conducted by numerically simulating the same propeller, under several operating conditions and blockages. Three test cases, using two propellers, were studied and some conclusions can be inferred:

- The adopted physical model is satisfactory and validated with experimental results;
- Glauert's correction seems to properly correct the K_T , K_Q , and η_0 due to the blockage effect. Even in moderate cavitation, observed when blockage increase thrust, the correction seems to be adequate on these coefficients;
- In extreme cases, notably when cavitation is extreme (covering 70% of P104's suction face or 28% of P107's suction faces), blockage may decrease the thrust. In these cases, blockage correction is not recommended;
- Thrust from suction face increases as the blockage increases. From the pressure face and hub, decreases as the blockage increases;
- Cavitation is also sensitive to blockage, and the percentage of the suction face covered by cavitation is not accurately corrected by Glauert's formula;
- The blockage ratio of 20% is the maximum blockage ratio that can be suggested in the experiments to study cavitation patterns.

For future works, new experiments using the same propeller in different cavitation tunnels, with different blockage ratios, would reassure the discussion here presented. Simulating more propellers, with different characteristics, would allow checking if the recommendation of blockage ratio lower than 20% is still acceptable for cavitation pattern experiments. It is expected that this work stimulates future studies in the area of blockage effects under presence of cavitation. Regarding the numerical model, a further investigation of different numerical models or estimate the numerical uncertainties considering the unsteadiness of the problem, by also analyzing the time-step, could be welcoming.

Acknowledgments

The authors thank Felipe Santos de Castro for the proofreading. Also, the authors thank Ricardo Sbragio and Helio Corrêa da Silva Junior for allowing the use of the propeller P107 data in this work. The first author thanks the Institute for Technological Research (IPT) and the Foundation for the Institute for Technological Research (FIPT). The last author thanks the financial support of CNPq (National Council for Scientific and Technological Development)

411 under grants 456359/2013-3 and 456345/2013-2; and the Brazilian Innovation Agency (FINEP) under grant CT-Infra-
412 01.18.0082.00.

413 References

- 414 Zilic de Arcos, F., Tampier, G., Vogel, C.R., 2020. Numerical analysis of blockage correction methods for tidal turbines. *Journal of Ocean*
415 *Engineering and Marine Energy* 6, 183–197. URL: <https://doi.org/10.1007/s40722-020-00168-6>[https://link.springer.com/](https://link.springer.com/10.1007/s40722-020-00168-6)
416 [10.1007/s40722-020-00168-6](https://doi.org/10.1007/s40722-020-00168-6), doi:10.1007/s40722-020-00168-6.
- 417 ASME, 2009. Standard for Verification and Validation in Computational Fluid Dynamics and Heat Transfer. Technical Report. The American Soci-
418 ety of Mechanical Engineers. URL: [https://www.asme.org/products/codes-standards/v-v-20-2009-standard-verification-](https://www.asme.org/products/codes-standards/v-v-20-2009-standard-verification-validation)
419 [validation](https://www.asme.org/products/codes-standards/v-v-20-2009-standard-verification-validation).
- 420 Balachandar, R., Ramamurthy, A.S., 1991. Blockage Effects on Cavitation Inception Characteristics of Bluff Bodies. *Proceedings of the Institution*
421 *of Mechanical Engineers, Part C: Mechanical Engineering Science* 205, 415–419. URL: [http://journals.sagepub.com/doi/10.1243/](http://journals.sagepub.com/doi/10.1243/PIME_PROC_1991_205_139_02)
422 [PIME_PROC_1991_205_139_02](http://journals.sagepub.com/doi/10.1243/PIME_PROC_1991_205_139_02), doi:10.1243/PIME_PROC_1991_205_139_02.
- 423 Barlow, J.B., Rae, W.H., Pope, A., 1999. *Low-Speed Wind Tunnel Testing*. Wiley. URL: [https://books.google.com.br/books?id=](https://books.google.com.br/books?id=nUHWdAAQBAJ)
424 [nUHWdAAQBAJ](https://books.google.com.br/books?id=nUHWdAAQBAJ).
- 425 BIPM, I., IFcc, I., IUPAC, I., ISO, O., 2012. International vocabulary of metrology – Basic and general concepts and associated terms (VIM).
426 *JcGM 200*, 2012. URL: https://www.bipm.org/utis/common/documents/jcgm/JCGM_200_2012.pdf.
- 427 Branlard, E., Meyer Forsting, A.R., . Assessing the blockage effect of wind turbines and wind farms using an analytical vortex model. *Wind Energy*
428 23, 2068–2086. URL: <https://onlinelibrary.wiley.com/doi/abs/10.1002/we.2546>, doi:<https://doi.org/10.1002/we.2546>,
429 [arXiv:https://onlinelibrary.wiley.com/doi/pdf/10.1002/we.2546](https://onlinelibrary.wiley.com/doi/pdf/10.1002/we.2546).
- 430 Choi, J.K., Kinnas, S.A., 1999. Numerical model of cavitating propeller inside of a tunnel. *Journal of Fluids Engineering, Transactions of the*
431 *ASME* 121, 297–304. doi:10.1115/1.2822207.
- 432 Collin, C., Mack, S., Indinger, T., Mueller, J., 2016. A Numerical and Experimental Evaluation of Open Jet Wind Tunnel Interferences using the
433 *DrivAer Reference Model*. *SAE International Journal of Passenger Cars - Mechanical Systems* 9, 657–679. doi:10.4271/2016-01-1597.
- 434 Dantas, J.L.D., Guedes, D.L., Kleine, F.A.S., Saggin, A.L.R., Katsuno, T., de Souza, J.M.P., Monteiro, T.G., Zanutto, J.C., Padovezi, C.D.,
435 2014. Modernização do Túnel de Cavitação do Instituto de Pesquisas Tecnológicas de São Paulo, in: 25º Congresso Nacional de Transporte
436 *Aquaviário, Construção Naval e Offshore, SOBENA - Sociedade Brasileira de Engenharia Naval*, Rio de Janeiro.
- 437 Deters, R.W., Ananda Krishnan, G.K., Selig, M.S., 2014. Reynolds Number Effects on the Performance of Small-Scale Propellers, in: 32nd
438 *AIAA Applied Aerodynamics Conference*, American Institute of Aeronautics and Astronautics, Reston, Virginia. pp. 1–43. URL: [http:](http://arc.aiaa.org/doi/10.2514/6.2014-2151)
439 [//arc.aiaa.org/doi/10.2514/6.2014-2151](http://arc.aiaa.org/doi/10.2514/6.2014-2151), doi:10.2514/6.2014-2151.
- 440 Eça, L., Hoekstra, M., 2014. A procedure for the estimation of the numerical uncertainty of CFD calculations based on grid refinement studies.
441 *Journal of Computational Physics* 262, 104–130. doi:10.1016/j.jcp.2014.01.006.
- 442 Espina-valdés, R., Fernández-jiménez, A., Francos, J.F., Blanco, E., Álvarez-álvarez, E., 2020. Small cross-flow turbine: design and testing in high
443 blockage conditions. *Energy Conversion and Management* 213. doi:10.1016/j.enconman.2020.112863.
- 444 Fischer, O., Kuthada, T., Mercker, E., Wiedemann, J., Duncan, B., 2010. CFD approach to evaluate wind-tunnel and model setup effects on
445 aerodynamic drag and lift for detailed vehicles. *SAE Technical Papers* doi:10.4271/2010-01-0760.
- 446 Gawn, R., Burrill, L., 1957. Effect of cavitation On the Performance of a Series of 16-Inch Model Propellers. *Institution of Naval Architects*.
- 447 Glauert, H., 1983. *The Elements of Aerofoil and Airscrew Theory*. volume 236. Cambridge University Press, Cambridge.
448 URL: <http://linkinghub.elsevier.com/retrieve/pii/S0016003243912141>[http://ebooks.cambridge.org/ref/id/](http://ebooks.cambridge.org/ref/id/CB09780511574481)
449 [CB09780511574481](http://ebooks.cambridge.org/ref/id/CB09780511574481)<https://www.cambridge.org/core/product/identifier/9780511574481/type/book>, doi:10.1017/
450 [CB09780511574481](https://www.cambridge.org/core/product/identifier/9780511574481/type/book).

451 Groves, N.C., Huang, T.T., Chang, M.S., 1989. Geometric characteristics of DARPA (Defense Advanced Research Projects Agency) SUBOFF
452 models (DTRC model numbers 5470 and 5471). Technical Report. David Taylor Research Center Bethesda MD Ship Hydromechanics Dept.

453 ITTC, 2011a. ITTC - Recommended Procedures and Guidelines - Resistance Test (7.5-02-02-01). Technical Report. ITTC. URL: [ittc.info/
454 media/1217/75-02-02-01.pdf](http://ittc.info/media/1217/75-02-02-01.pdf).

455 ITTC, 2011b. ITTC – Recommended Procedures: Fresh Water and Seawater Properties. Technical Report. ITTC. URL: [ittc.info/media/
456 1215/75-02-01-03.pdf](http://ittc.info/media/1215/75-02-01-03.pdf), doi:10.1002/cphc.200400116.

457 ITTC, 2016. ITTC – Recommended Procedures and Guidelines ITTC Quality System Manual Recommended Procedures and Guidelines Cavi-
458 tation Induced Erosion on Propellers , Rudders and Appendages Model Scale Experiments ITTC – Recommended Procedures and Guidelines
459 Cavitation. Technical Report. ITTC.

460 ITTC, 2017. ITTC – Recommended Procedures and Guidelines - Model - Scale Cavitation Test (7.5-02-03-03.1). Technical Report. ITTC.

461 JCGM, J., et al., 2008. Evaluation of measurement data—Guide to the ex pression of uncertainty in measurement. Bureau International des Poids
462 et Mesures URL: https://www.bipm.org/utils/common/documents/jcgm/JCGM_100_2008_E.pdf.

463 Katsuno, E.T., Dantas, J.L.D., 2017. Analysis of the Blockage Effect on a Cavitation Tunnel Using CFD Tools, in: Volume 7B: Ocean Engineer-
464 ing, ASME. p. V07BT06A043. URL: [http://proceedings.asmedigitalcollection.asme.org/proceeding.aspx?doi=10.1115/
465 OMAE2017-61545](http://proceedings.asmedigitalcollection.asme.org/proceeding.aspx?doi=10.1115/OMAE2017-61545), doi:10.1115/OMAE2017-61545.

466 Lee, H.S., Kinnas, S.A., 2005. A BEM for the modeling of unsteady propeller sheet cavitation inside of a cavitation tunnel. Computational Me-
467 chanics 37, 41–51. URL: <https://linkinghub.elsevier.com/retrieve/pii/S0960148114007873>[http://link.springer.com/
468 10.1007/s00466-005-0696-z](http://link.springer.com/10.1007/s00466-005-0696-z), doi:10.1007/s00466-005-0696-z.

469 Ljungskog, E., Sebben, S., Broniewicz, A., 2020. Journal of Wind Engineering & Industrial Aerodynamics Inclusion of the physical wind tunnel
470 in vehicle CFD simulations for improved prediction quality. Journal of Wind Engineering & Industrial Aerodynamics 197, 104055. URL:
471 <https://doi.org/10.1016/j.jweia.2019.104055>, doi:10.1016/j.jweia.2019.104055.

472 Meng, N., Hu, X., Tian, M., 2020. Effect of blockage on critical ventilation velocity in longitudinally ventilated tunnel fires. Tunnelling and
473 Underground Space Technology 106, 103580. URL: <https://doi.org/10.1016/j.tust.2020.103580>, doi:10.1016/j.tust.2020.
474 103580.

475 Menter, F.R., 1994. Two-equation eddy-viscosity turbulence models for engineering applications. AIAA Journal 32, 1598–1605. URL: [http:
476 //arc.aiaa.org/doi/10.2514/3.12149](http://arc.aiaa.org/doi/10.2514/3.12149), doi:10.2514/3.12149.

477 Mikkelsen, R.F., Sørensen, J.N., 2002. Modelling of Wind Tunnel Blockage, in: 15th IEA Symposium on the Aerodynamics of Wind Turbines,
478 FOI Swedish Defence Research Agency.

479 Ross, H., Polage, B., 2020. An experimental assessment of analytical blockage corrections for turbines. Renewable Energy 152, 1328–1341.
480 URL: <https://doi.org/10.1016/j.renene.2020.01.135>, doi:10.1016/j.renene.2020.01.135.

481 Ryi, J., Rhee, W., Hwang, U.C., Choi, J.S., 2015. Blockage effect correction for a scaled wind turbine rotor by using wind tunnel test data.
482 Renewable Energy 79, 227–235. URL: <http://dx.doi.org/10.1016/j.renene.2014.11.057>, doi:10.1016/j.renene.2014.11.057.

483 Sauer, J., Schnerr, G.H., 2001. Development of a New Cavitation Model based on Bubble Dynamics. ZAMM - Journal of Applied Mathematics
484 and Mechanics / Zeitschrift für Angewandte Mathematik und Mechanik 81, 561–562. URL: [https://onlinelibrary.wiley.com/doi/
485 10.1002/zamm.20010811559](https://onlinelibrary.wiley.com/doi/10.1002/zamm.20010811559), doi:10.1002/zamm.20010811559.

486 Sbragio, R., 1995. Projeto Racional de Propulsores de Alto Skew. Master’s thesis. University of São Paulo, Escola Politécnica.

487 Segalini, A., 2021. An analytical model of wind-farm blockage. Journal of Renewable and Sustainable Energy 13, 033307.

488 Shirzadeh, K., Hashemi, P., Gharali, K., Zandi, M., 2021. Development of a wind turbine simulator to design and test micro HAWTs. Sustainable
489 Energy Technologies and Assessments 43, 100900. URL: <https://doi.org/10.1016/j.seta.2020.100900>, doi:10.1016/j.seta.
490 2020.100900.

491 Siemens, 2018. STAR-CCM+ Documentation - version 13.06.

492 Sorensen, J.N., Shen, W.Z., Mikkelsen, R., 2006. Wall Correction Model for Wind Tunnels with Open Test Section. AIAA Journal 44, 1890–1894.
493 URL: <https://arc.aiaa.org/doi/10.2514/1.44602><https://arc.aiaa.org/doi/10.2514/1.15656>, doi:10.2514/1.15656.

- 494 Soto-Valle, R., Alber, J., Manolesos, M., Nayeri, C.N., Paschereit, C.O., 2020. Wind Turbine Tip Vortices under the influence of Wind Tunnel
495 Blockage Effects. *Journal of Physics: Conference Series* 1618. doi:10.1088/1742-6596/1618/3/032045.
- 496 Watanabe, S., Brennen, C.E., 2003. Dynamics of a Cavitating Propeller in a Water Tunnel. *Journal of Fluids Engineering* 125,
497 283–292. URL: [https://asmedigitalcollection.asme.org/fluidsengineering/article/125/2/283/463196/Dynamics-of-](https://asmedigitalcollection.asme.org/fluidsengineering/article/125/2/283/463196/Dynamics-of-a-Cavitating-Propeller-in-a-Water)
498 [a-Cavitating-Propeller-in-a-Water](https://asmedigitalcollection.asme.org/fluidsengineering/article/125/2/283/463196/Dynamics-of-a-Cavitating-Propeller-in-a-Water), doi:10.1115/1.1524588.
- 499 Wimshurst, A., Vogel, C., Willden, R., 2018. Cavitation limits on tidal turbine performance. *Ocean Engineering* 152, 223–233. URL: <https://doi.org/10.1016/j.oceaneng.2018.01.060>, doi:10.1016/j.oceaneng.2018.01.060.
500